Contrib Mineral Petrol (2015) 170:11
DOI 10.1007/s00410-015-1168-x

ORIGINAL PAPER

Genesis of the central zone of the Nolans Bore rare earth element deposit, Northern Territory, Australia

Louise Schoneveld[1,3] · **Carl Spandler**[1] · **Kelvin Hussey**[2]

Received: 2 February 2015 / Accepted: 28 June 2015 / Published online: 21 July 2015

Abstract The Nolans Bore rare earth element (REE) deposit consists of a network of fluorapatite-bearing veins and breccias hosted within Proterozoic granulites of the Reynolds Range, Central Australia. Mineralisation is divided into three zones (north, central, and south-east), with the north and south-east zones consisting of massive REE-bearing fluorapatite veins, with minor brecciation and carbonate infill. The central zone is distinctively different in mineralogy and structure; it features extensive brecciation, a high allanite content, and a large, epidote-rich enveloping alteration zone. The central zone is a reworking of the original solid apatite veins that formed during the Chewings Orogeny at ca. 1525 Ma. These original apatite veins are thought to derive from phosphate-rich magmatic–hydrothermal fluid exsolved from as-yet unrecognised alkaline magmatic bodies at depth. We define four ore breccia types (BX1–4) in the central zone on the basis of detailed petrological and geochemical analysis of drillcore and thin sections. BX1 ore comprises fluorapatite with minor crackle brecciation with carbonate infill and resembles ore of the north and south-east zones. Breccia types BX2, BX3, and BX4 represent progressive stages of ore brecciation and development of calc-silicate mineral (amphibole, epidote, allanite, calcite) infill. Comparison of bulk ore sample geochemistry between breccia types indicates that REEs were not mobilised more than a few centimetres during hydrothermal alteration and brecciation. Instead, most of the REEs were partitioned from the original REE fluorapatite into newly formed allanite, REE-poor fluorapatite and minor REE carbonate in the breccias. Negative europium (Eu) anomalies in the breccia minerals are accounted for by a large positive Eu anomaly in epidote from the alteration zones surrounding the ore breccias. This observation provides a direct link between ore recrystallisation and brecciation, and the formation of the alteration halo in the surrounding host rocks. Where allanite and fluorapatite are texturally related, the fluorapatite is relatively depleted in the light rare earth elements (LREEs), whereas allanite is relatively LREE enriched, suggesting co-crystallisation. We tentatively date the BX1 ore stage to 1440 ± 80 Ma based on U–Pb dating of thorianite. Sm–Nd isotope isochrons derived from in situ isotope analysis of cognate apatite and allanite date the BX2 and BX3 events to ca. 400 Ma, while U–Pb dating of late-stage monazite from the BX4 ore stage returned an age of ca. 350 Ma. Therefore, formation of the central zone at Nolans Bore involved multiple alteration/brecciation events that collectively span over 1 billion years in duration. We suggest that the BX1-type veins and breccias were formed from REE-rich, saline (F- and Cl-bearing) fluids that infiltrated the granulite-grade host rocks in association with either shear activation events of the Redbank Shear Zone (1500–1400 Ma) or intrusion of late-stage pegmatites of the Mt Boothby area. BX2, BX3, and BX4 events record deformation and hydrothermal alteration associated with the Alice Springs Orogeny

Communicated by Chris Ballhaus.

Electronic supplementary material The online version of this article (doi:10.1007/s00410-015-1168-x) contains supplementary material, which is available to authorized users.

✉ Louise Schoneveld
louise.schoneveld@anu.edu.au

[1] Economic Geology Research Centre (EGRU), James Cook University, Townsville, QLD 4811, Australia

[2] Arafura Resources Ltd., Darwin, Northern Territory, Australia

[3] Present Address: Research School of Earth Sciences, Australian National University, Acton, ACT 2601, Australia

(400–350 Ma). These hydrothermal events occurred at temperatures of 450 to ~600 °C, due to inflow of highly acidic hydrous fluids derived from a magmatic source, or from mixing of meteoric and metamorphic fluids. Our data testify to the long and complex geological history of not only the Nolans Bore REE deposit, but also of the rocks of the eastern Reynolds Range, and demonstrate the great utility of using hydrothermally derived REE minerals to trace the timing of crustal deformation events and source of associated hydrothermal fluids.

Keywords Rare earth elements · Fluorapatite · Allanite · Nolans Bore · Ore deposit · Sm–Nd isotopes

Introduction

Globally, there are few rare earth element (REE) ore deposits that can wholly be regarded as hydrothermal, which is likely a consequence of the relative immobility of these elements in most common hydrothermal fluids (Haas et al. 1995; Williams-Jones et al. 2012). Instead, most of the world's REEs are currently supplied from ore deposits related to carbonatite or alkaline magmatism (Chakhmouradian and Zaitsev 2012). For this reason, it may be expected that landmasses lacking significant alkaline or carbonatitic igneous rocks, such as Australia, would not be well suited for hosting REE mineralisation, yet Australia hosts several world class REE ore deposits, including Nolans Bore.

Nolans Bore is a hydrothermal REE deposit located 135 km north-west of Alice Springs in the Northern Territory, Australia (Huston et al. 2011). The deposit, held by Arafura Resources Ltd., is a stockwork vein-style deposit, containing 47 Mt of identified mineral resource at 2.6 % rare earth oxides (REO) (Hussey and Tyrrell 2012). Unlike most REE deposits, the main ore mineral is fluorapatite that is found in thick veins or breccia zones cutting granulite-grade gneisses and metasediments (Hoatson et al. 2011). Despite the rather unique characteristics of Nolans Bore, there has been little previous research on the deposit. Recently, Huston et al. (2011, 2015) examined the solid apatite veins of the north zone of the deposit and presented a geological model for ore formation. Here, we examine the central zone of the deposit that consists of variably brecciated and deformed ore, enveloped by a broad hydrothermal alteration halo. We document the paragenesis and mineralogy of the orebody, and present bulk-rock and mineral geochemistry, oxygen isotope mineral compositions, and geochronological data (U–Pb and Sm–Nd) to help understand the origin and evolution of the mineralisation. Our work not only enhances geological understanding of this unique ore deposit, but also contributes to the knowledge of the geological evolution of the Reynolds Range and our understanding of how REEs are mobilised and precipitated by crustal fluids.

Regional geology

Nolans Bore is located in the >70-km-long, north-west-trending Reynolds Range that occupies a small section of the 200,000 km^2 Arunta Region of Central Australia (Fig. 1, inset; Rubatto et al. 2001). The metamorphic grade of the Reynolds Range increases along the strike from greenschist in the north-west to granulite in the south-east (Vry et al. 1996; Rubatto et al. 2001). The region has undergone a complex history with major periods of geological activity being concentrated in the Paleo-Mesoproterozoic and Paleozoic eras (Roberts and Houseman 2001; Hussey 2003; Claoué-Long et al. 2008). In chronological order, the most significant geological events to affect the Arunta region are:

1. 1840–1810 Ma—Deposition of the Lander Rock Formation: a thick package of turbidite-related mudstones and sandstones (Claoué-Long et al. 2008; Raimondo et al. 2011).
2. 1810–1800 Ma—the Stafford Event: marked by bimodal magmatism and tight folding of the Lander Rock Formations (Claoué-Long and Hoatson 2005; Worden et al. 2008).
3. 1810–1780 Ma—Deposition of the Reynolds Range Group during crustal extension. This sedimentary package primarily consists of quartzite, calc-silicate, and pelite units (Dirks 1990; Buick and Cartwright 1996; Claoué-Long et al. 2008).
4. 1790–1770 Ma—the Yambah Event: interpreted as the closure of a back-arc basin synchronous with emplacement of many large granite bodies, such as the Napperby Gneiss (Scrimgeour 2006; Hoatson et al. 2011; Raimondo et al. 2011).
5. 1740–1690 Ma—the Strangway Orogeny: a long-lived event of high-grade metamorphism and localised granite intrusions. The end of this event is marked by regional extension and intrusion of the Strangways Range dolerite dyke swarm at ca. 1690 Ma (Shaw et al. 1984; Claoué-Long and Hoatson 2005; Claoué-Long et al. 2008).
6. 1600–1520 Ma—the Chewings Orogeny: in the Reynolds Range, this event caused a metamorphic overprint, ranging from greenschist facies (ca. 400 °C) in the north-west to granulite facies (0.4–0.7 GPa, 700 to >850 °C) with associated anatexis and deformation in the south-east (Dirks et al. 1991; Claoué-Long et al. 2008; Anderson et al. 2013; Morrissey et al. 2014). The high temperature and duration (ca. 60–80 m.y.) of metamorphism is suggested to be caused by deep-

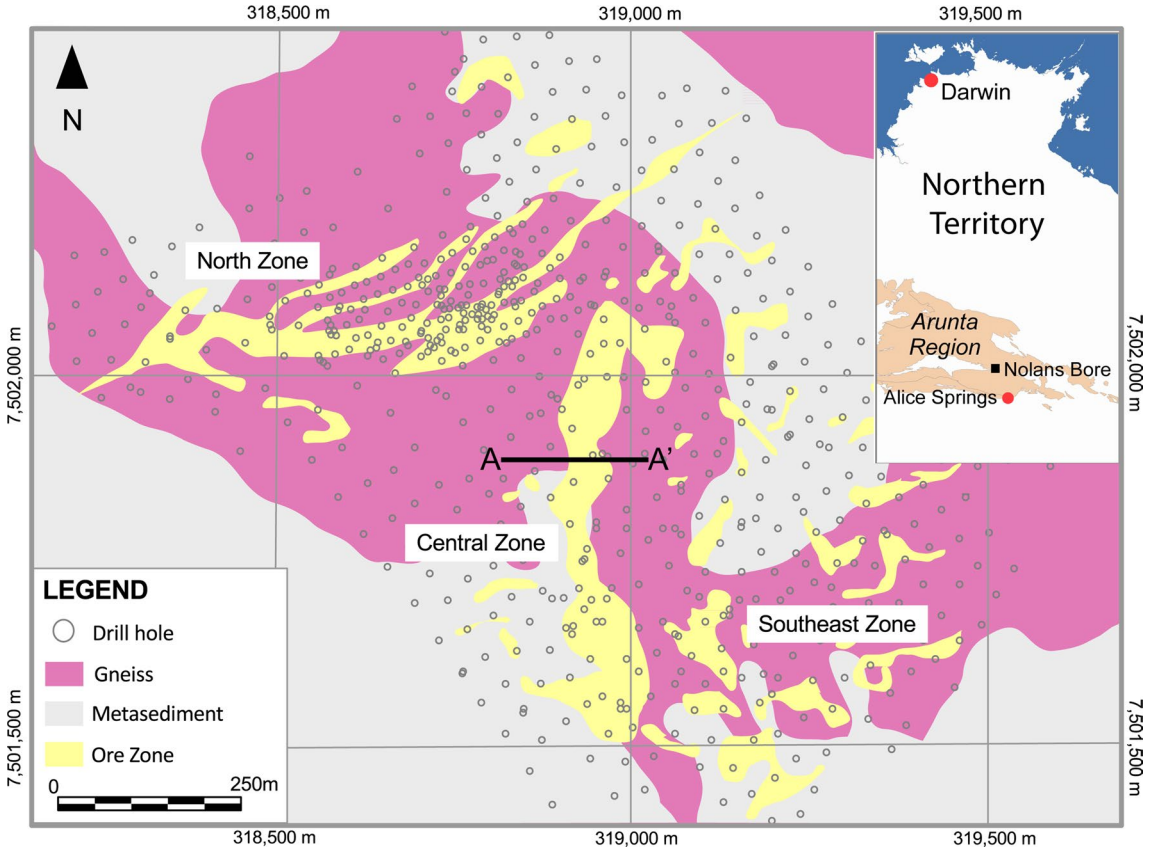

Fig. 1 Drill grid and sub-surface geology map of the Nolans Bore ore deposit. The ore zones are defined as units with >0.5 % REO (modified from Hussey and Tyrrell (2012)). A–A′ cross section is the main investigation area for the central zone. *Inset*: location of Nolans Bore in the Northern Territory, Australia

seated high-heat-producing granites (Rubatto et al. 2001; Anderson et al. 2013; Morrissey et al. 2014), although there is no known magmatism of significance correlated with this event (Scrimgeour 2006). Nevertheless, Anderson et al. (2013) and Morrissey et al. (2014) suggest that the late pegmatites at Mt Boothby, dated at 1523 ± 8 Ma and 1513 ± 15 Ma, also belong to the Chewings Orogeny as there is no other evidence of a thermal event at this age. These ages also correlate with the expected age of the primary mineralisation at Nolans Bore (ca. 1525 Ma, from allanite; Huston et al. 2015), which is located less than 10 km west of Mt Boothby.

7. 1500–1400 Ma—the Redbank Shear Zone: an extensive shear event with a strike length of 400–500 km that is estimated to have offset the Moho by 20 km. Shearing was associated with the development of hydrated mylonitic fabrics, and temperatures are estimated to have reached 550–650 °C (Shaw and Black 1991; Hand and Sandiford 1999). However, the effects of this event are not restricted to shear zones, as resetting of isotopic systems is documented across the belt at this time (Collins and Shaw 1995; Collins and Williams 1995; Buick and Cartwright 1996)
8. 450–300 Ma—the Alice Springs Orogeny: the youngest tectonic event to affect the Reynolds Range region (Roberts and Houseman 2001; Claoué-Long et al. 2008; Raimondo et al. 2011). This intraplate orogenic event is deemed to be responsible for most of the current topography and the current juxtaposition of granulite and greenschist facies Proterozoic rocks in the region (Claoué-Long and Hoatson 2005). Tectonic activity involved north–south shortening, most of which was accommodated by deformation and uplift of the region via the reactivation of the Redbank Shear Zone (Hand and Sandiford 1999; Roberts and Houseman 2001) and initiation of other large (>100 m wide) hydrous shear zones (Collins and Teyssier 1989; Raimondo et al. 2011; Anderson et al. 2013). Thermobarometry studies estimate the conditions of metamorphism in the Reynolds Ranges during the Alice Springs Orogeny reached ca. 530 °C and 0.4–0.5 GPa (Raimondo et al. 2011). There is no known magmatism related to this event.

Deposit geology

Nolans Bore is poorly exposed as it is covered by up to 4 m of alluvium, so geological characterisation of the deposit has been defined almost solely from logging and analysis of drillcore recovered from extensive drilling programs. The identified mineral resource is confined to an area of 1.5 km by 1.2 km from the surface down to at least 220 m vertical depth, with the full extent of the deposit yet to be defined. The REEs are hosted in four main ore types: (1) massive fluorapatite veins, (2) high-grade cheralite-bearing, apatite-poor kaolinitic zones, (3) apatite–allanite–epidote zones hosted in brecciated calc-silicate rocks, and (4) low-grade stockwork zones. The deposit is divided into three areas: the north zone, the central zone, and the south-east zone (Fig. 1). The north and south-east ore zones are primarily ore type 1, while the central zone is largely made up of ore type 3.

North and south-east ore zones

Most of the REE mineralisation found in the north and south-east zones occurs as steeply north-dipping, north-east-trending fluorapatite veins with 4–6 % rare earth oxides (Hoatson et al. 2011) that are hosted within the Boothby orthogneiss (Fig. 1). The north zone and the primary mineralisation conditions are described in detail by Huston et al. (2011, 2015). These original solid apatite veins are suggested to have been formed from phosphate-rich magmatic–hydrothermal fluid exsolved from crystallising alkaline intrusion emplaced at deeper crustal levels. These veins are dominated by coarse pale-yellow apatite grains with subordinate quartz, allanite, calcite, and REE-rich carbonates and are surrounded by relatively thin (<1 m) alteration selvages consisting of clinopyroxene and amphibole, with or without garnet, K-feldspar, quartz, and calcite. The veins are expected to have precipitated from the mineralising fluid due to local fluid–rock interaction, and/or fluid mixing and decompression at around 400 °C (Huston et al. 2015).

Ore types of the central zone

The central zone is distinguished from the other zones by the distinct north–south trend of the ore lens, the highly brecciated nature and relatively high allanite content of the ore, and the broad quartz + epidote ± amphibole alteration envelope. This mineralisation style is only found in small quantities in other sections of the deposit. The main ore horizon dips steeply to the east (Fig. 2) and is focused along, or close to, the contact between the Boothby granitic gneiss (to the east) and metasedimentary rocks of the Landers Group (to the west), both of which experienced granulite facies metamorphism during the Strangways Orogeny at ca. 1740–1690 Ma (Scrimgeour 2006; Claoué-Long et al. 2008). The contact between the orthogneiss and underlying metasediments is intensely deformed and sheared, even in areas free of mineralisation and related alteration (Fig. 2). Detailed logging of core from seven drillholes was conducted to characterise the ore styles and structural relationships of the central zone (Fig. 2). The core logging reveals that continuity of ore types and structures is less than 2 m in many cases, although REE grade is relatively uniform across the zone. We identified four main types of brecciated fluorapatite-bearing ore, herein labelled BX1–BX4 (Fig. 3).

BX1 apatite breccia

The BX1 ore type occurs primarily as two relatively continuous vein structures located within the granitic gneiss and in the metasedimentary rocks in the hanging wall and footwall to the main ore intersection, respectively (Fig. 2). The BX1 veins are generally between 0.1 and 5 m thick, but can reach up to 20 m thick in the deepest section of the deposit. Alteration of the host rocks around these BX1 veins is limited to relatively thin (~0.1–0.5 m thick) zones dominated by pyroxene and garnet.

BX1-type ore is cream in colour with crackle to mosaic brecciation and is defined by fluorapatite clasts with less than 10 % infill. The fluorapatite clasts tend to be angular to sub-rounded and can range from 0.5 to 50 mm in size (Fig. 3). Apatite and calcite are the dominant infill minerals, but REE-Ca-carbonates (Fig. 4a) and allanite may also be present. Microscale backscattered electron imaging reveals that the fluorapatite grains contain complex irregular zoning features and contain abundant minute mineral inclusions of thorite, monazite, and REE-Ca-carbonates (Fig. 4a). Small sections of this breccia type also feature sparse but coarse (ca. 5 mm) euhedral thorianite (ThO_2) grains (Fig. 8a) that were targeted for in situ U–Pb dating, as outlined below.

BX2 apatite breccia

BX2-type ore is a crackle to mosaic breccia and is defined by allanite (± calcite) infill around fluorapatite clasts (Fig. 3). The infill can constitute up to 20 % of the breccia volume and commonly manifests as veinlets that rarely exceed 2 mm in width (Fig. 4b). These allanite veinlets are confined to the fluorapatite and do not continue to the surrounding rocks.

BX3 apatite breccia

BX3 breccia is defined by fluorapatite clasts in a black infill that consists of various amounts of allanite and amphibole (Fig. 3). BX3 is dominated by rubble breccia that is generally

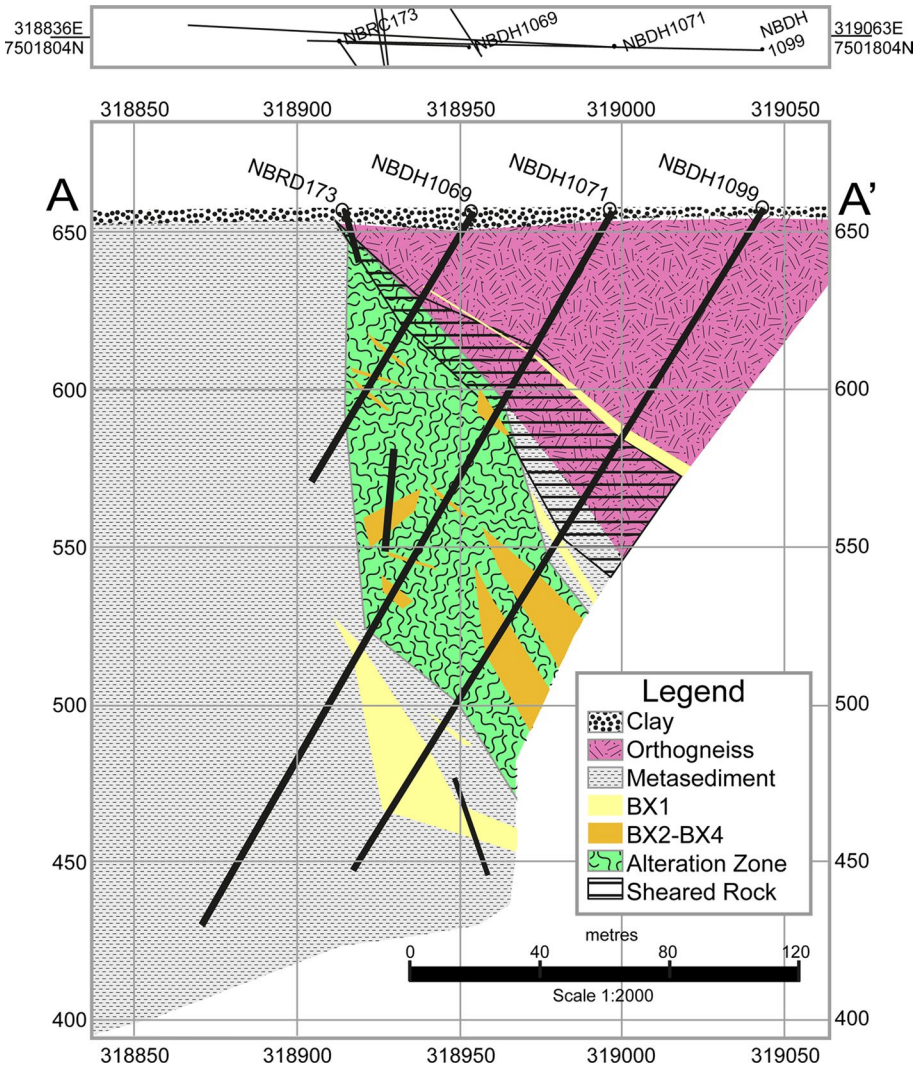

Fig. 2 East–west schematic cross section of the central zone of Nolans Bore along 7501804N (Line trace A–A′ in Fig. 1). The surface lies at >650 m above sea level. This cross section incorporates the entire drilled length of drillholes NBDH1099, NBDH1071, NBDH1069 and also incorporates parts of four other holes that intersect, or nearly intersect, this section, as shown in the birds eye schematic plan section above the cross section

matrix supported. The fluorapatite clasts are usually subrounded to angular, but have been observed with resorbed edges or euhedral forms. These clasts can contain thin allanite crackle veinlets, or up to 100-μm allanite inclusions. The clasts range from 2 to 100 mm and are poorly sorted. The infill constitutes 10–80 % of rock volume and is fine grained. In many cases, spectacularly zoned REE epidote/allanite crystals have overgrown fluorapatite clasts (Fig. 4c), whereas in other cases, apatite clasts feature an inclusion-free rim (~500 μm) and an allanite-inclusion-rich core (Figs. 4d, 8c). This rock type is often enveloped by small (up to 5 cm) amphibole-only alteration selvages that transition into broader epidote–quartz alteration zones (see below).

BX4 apatite breccia

BX4 breccia is the least common of all the breccia types: it is predominantly an angular rubble breccia with 50–70 % matrix and little infill. BX4 has multiple mineral clast types including fluorapatite, amphibole, epidote, and pyroxene with a matrix of the same mineral assemblage (Fig. 4e) plus rare phlogopite, and late-stage infill of REE carbonate and monazite (Fig. 4f).

The BX2, BX3, and BX4 breccia types comprise the bulk of the ore in the central zone. These breccia types are located in a quartz + epidote ± amphibole alteration envelope that lies immediately on, or below, the gneiss metasedimentary rock contact (Fig. 2). There is a gradual transition between BX2 and BX3 type ores when they occur adjacently. The BX4-type breccia is localised to very small sections (<2 m) and occurs commonly in the sheared zone between the metasediment and overlying gneiss.

Alteration zones

In most cases, the ore lenses in the central zone are enveloped by alteration zones that extend into the host rocks. Surrounding the BX2, BX3, and BX4 ore types are broad (up 50 m thick) epidote–quartz (± amphibole) alteration zones (Fig. 5a) that grade into sheared amphibole-rich

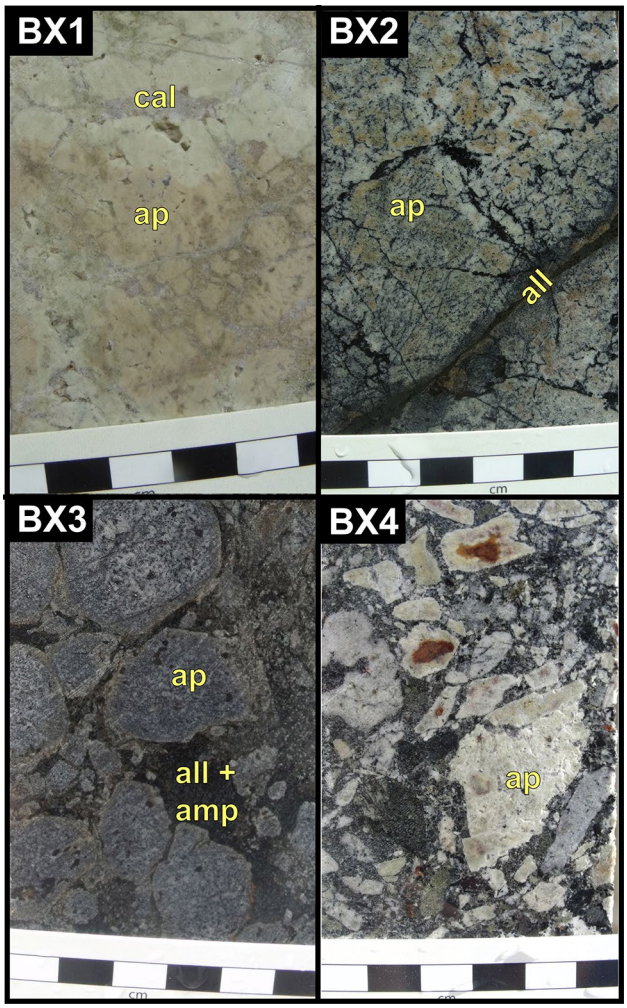

Fig. 3 Representative samples of each breccia type. Each block on the *scale bar* is 1 cm. *(BX1)* Cream fluorapatite with minor calcite crackle brecciation, located in NBDH1095 at 240 m (sample A46). *(BX2)* Fluorapatite with allanite crackle brecciation, located in NBDH1099 at 145.5 m. *(BX3)* Rubble breccia with fluorapatite clasts and a black infill comprising a mixture of amphibole and allanite, located in NBDH1099 at 143.1 m (sample A8). *(BX4)* Angular rubble breccia. Clasts include fluorapatite, amphibole, allanite, and epidote with a matrix of the same minerals and little infill, located in NBDH1099 at 125.0 m (sample A6). Abbreviation key: *all* allanite, *amp* amphibole, *ap* apatite, *cal* calcite

zones where in direct contact with BX3 type ore (Fig. 5b, c). A relatively thin clinopyroxene-rich alteration selvage is usually present between BX1 ore and host rock metasediments (Fig. 5d). These alteration rock types are described in more detail below.

Epidote–quartz alteration

Alteration zones consisting predominately of yellow-green epidote and quartz (Fig. 5a) are the dominant alteration type in this zone. Epidote and quartz are medium grained and are present in roughly equal proportions, although near pure epidote varieties occur in places, and actinolitic amphibole (Fig. 5b) becomes a major phase in proximity to the brecciated ore. Minor amounts of euhedral titanite (up to several mm in size) are commonly present, and trace chalcopyrite, fluorite, and apatite can be found.

Amphibole-rich alteration

This alteration type is distinguished by the dominance of foliated black actinolite. It commonly surrounds the BX3-type breccia and can extend up to 10 cm into the surrounding rock. The rock comprises fine- to coarse-grained actinolite (>80 modal %) that is often acicular or bladed in form and aligned parallel to the rock contacts. Minor but variable amounts of epidote, calcite, titanite, and apatite may be present in these zones. The boundary between the ore breccia and the alteration zone is transitional as the infill of BX3 also contains amphibole, whereas the contact between the amphibole alteration and the epidote–quartz-dominated alteration is usually sharp (Fig. 5c).

Clinopyroxene alteration

The contact between the BX1 breccia and metasedimentary rocks is marked by a thin (>10 cm) alteration zone dominated by light green/blue clinopyroxene (Fig. 5d). Contacts between these rock units are consistently sharp (Fig. 5d), with a rim of fine-grained allanite often forming along the contact between the alteration zone and BX1 breccia. The alteration zone contains medium to course, blocky grains of clinopyroxene (augite, see below) with trace amounts of calcite. These zones are distinguished from the alteration selvages found around the ore in the north zone by the rarity of garnet and feldspar.

Methods

Bulk-rock geochemical analysis

Bulk-rock chemical analysis was performed by Arafura Resources Ltd., as part of the drill program. In some cases, core samples were collected according to rock type; in other cases, the core was sampled in 1- or 2-m intervals irrespective of core lithology. Half core samples were analysed by Northern Territories Environmental Laboratories, Darwin, using ICP-MS/OES techniques, following a three-acid digest method. Precision and accuracy of the assay results were monitored through regular analysis of duplicates, laboratory blanks and blind analysis of certified reference standards, and Arafura in-house reference standards.

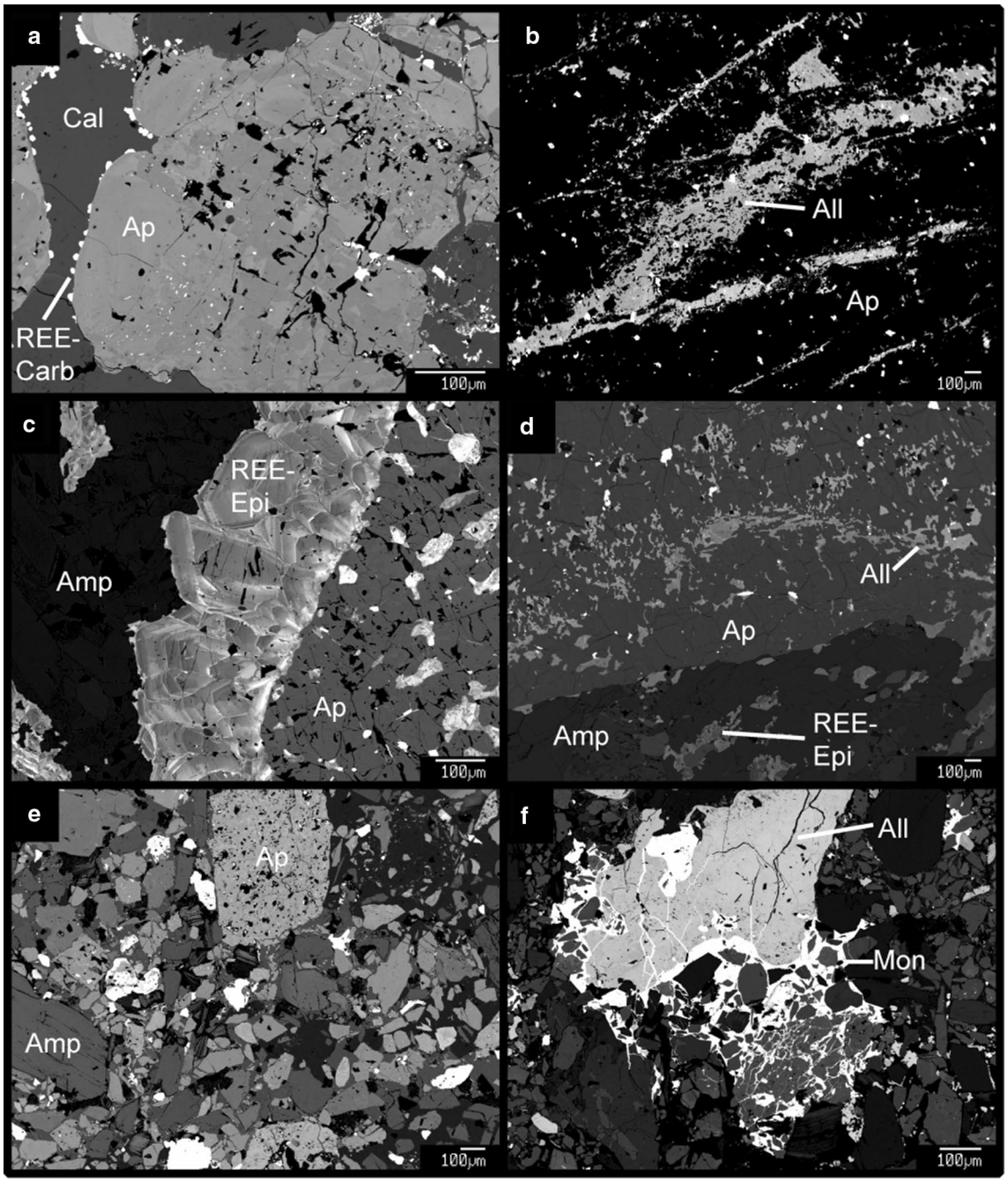

Fig. 4 Backscattered electron (BSE) images of breccia textures at the sub-mm scale. Note that the intensity of the BSE images has been adjusted for each image for optimal resolution of the phases of interest. **a** BX1 breccia with a fluorapatite clast containing cavities and micrometre-scale exsolutions. Calcite infill with REE-Ca-carbonate crystals (bright in BSE) developed on the margins of the fluorapatite grains; thin-section number A46—NBDH1095 at 246.51 m. **b** BX2 breccia with wormy allanite veining through fluorapatite; thin-section sample A49—NBDH1099 at 163.05 m. **c** BX3 showing REE-epidote overgrowth on a fluorapatite clast with amphibole infill; thin-section sample A33—NBRD104 at 163.21 m. **d** BX3 breccia. An apatite clast with allanite inclusions in an amphibole + REE-epidote matrix; thin-section sample A8—NBDH1099 at 143.04 m. **e** BX4 breccia with fluorapatite and amphibole clasts in a matrix of the same minerals, plus calcite and quartz infill; thin-section sample A6—NBDH1099 at 125.13 m. **f** BX4-type breccia displaying an allanite clast with monazite (bright phase is BSE) infill. This monazite was targeted for U–Pb dating; thin-section sample A6, see Fig. 12d. Abbreviation key: *all* allanite, *amp* amphibole, *ap* apatite, *cal* calcite, *mon* monazite, *REE-carb* REE-Ca-Carbonate mineral, *REE-Epi* REE-rich epidote

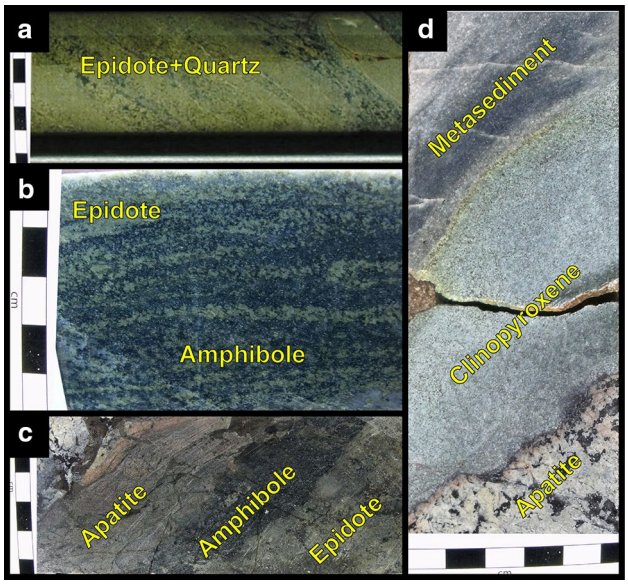

Fig. 5 Core photographs of alteration rock types. Each block on the *scale bar* represents ~1 cm. **a** Epidote–quartz alteration assemblage, with minor amphibole; sample location—NBRD104 at 149 m. **b** Epidote–amphibole alteration assemblage; sample location—NBDH1095 at 159 m. **c** Amphibole-rich alteration selvage between fluorapatite ore and epidote-dominated alteration zone; sample location—NBDH1095 at 129 m. **d** Clinopyroxene-rich alteration zone between BX1-type apatite veins and host rock metasediments; sample location—NBDH1071 at 154 m

Major element analysis of minerals

Mineral chemical analysis was carried out in situ on polished thin sections of core samples. Major element mineral analyses and X-ray element maps were acquired using a JEOL JXA8200 superprobe housed at the Advanced Analytical Centre (AAC), James Cook University (JCU), Townsville. Quantitative analysis of minerals was conducted by wavelength-dispersive spectrometry, using a 20-nA beam defocussed to 5 μm, with acceleration voltage set to 15 kV. All analyses were standardised using well-characterised silicate (for Si, Al, Ca, Mg, Fe, Na, K, Cl), oxide (for Ti, Mn, Fe), calcite (Ca), fluorite (Sr, F), and phosphate (for REE, Y, P) standards and applying ZAF corrections. All element measurements were taken on k-alpha X-ray lines, except La and Ce that were measured on l-alpha lines, and Pr and Nd, which used l-beta lines. We recognised a significant interference of a minor Ce peak on F, which returned excessive values for F contents in the REE-carbonate data. We were able to apply an offline correction to account for the Ce peak on F by measurement of F-free, Ce phosphate standards. We also performed X-ray mapping of several zoned REE-carbonate grains from BX1 (A2) and BX4 (A7) samples for La, Ce, and Nd.

Trace element analysis of minerals

In situ trace element analyses of minerals were conducted by laser ablation ICP-MS using a Geolas Pro 193-nm ArF excimer laser system coupled with a Bruker (formally Varian) 820–MS-ICP-MS at the AAC, JCU. The laser fluence was set to 6 J/cm^2 at the sample site with laser repetition rate set to 10 Hz and a beam diameter of between 32 and 44 μm. Ablation was conducted in a He atmosphere, which was subsequently mixed with Ar prior to introduction into the ICP-MS. The ICP-MS was tuned for robust plasma conditions (Th/U sensitivity ratio ~1) and low oxide production rates (ThO/Th < 0.5 %). The internal standard isotope used for data reduction was ^{43}Ca for fluorapatite, allanite, and epidote, and ^{139}La for REE carbonates, based on Ca and La contents measured previously by WDS. Thorianite analyses were quantified by summing all element oxides to 100 %. Qualitative trace element analysis of amphibole and pyroxene showed these minerals to have low REE contents, so these minerals were not subject to further analysis. NIST SRM 610 was used as a bracketing external standard using the standard reference values of Spandler et al. (2011).

Oxygen isotope analysis

Oxygen isotope analyses of minerals were conducted at the GNS Science Stable Isotope Laboratory, Lower Hutt, New Zealand. Oxygen was extracted from quartz, amphibole, and epidote mineral separates by CO_2 laser (Sharp 1990) using BrF_5 as the oxidising agent. The mineral grains were put into a sample chamber, which was then evacuated for approximately 2 h. Blank runs were done until oxygen yields were less than 0.1 μmol. After extraction, oxygen yields were recorded, and CO_2 gas was analysed on a Geo20–20 mass spectrometer. Values are reported in the familiar $\delta^{18}O$ notation, relative to VSMOW. The samples were normalised to the international quartz standard NBS-28 using a value of +9.6 ‰ and the garnet standard UWG-2 using a value of 5.8 ‰ (Valley et al. 1995). Values of standards varied by less than 0.1 per mil within each batch of samples. The analytical precision for these measurements is 0.1 ‰ $\delta^{18}O$.

In situ U–Pb isotope geochronology

During petrographic analysis of samples, we identified several minerals that were considered to be potentially suitable for in situ U–Pb dating, including allanite, titanite, thorianite, and monazite. Preliminary testing of titanite and allanite by LA-ICP-MS revealed these minerals to contain high levels of common Pb and, in the case of titanite, very low U contents. Therefore, these minerals were not subject to quantitative U–Pb dating analysis, although the qualitative

work did indicate formation ages of around 400–450 Ma. In contrast, both monazite and thorianite contained high U and Th contents and very low levels of common Pb, and returned inclusion-free, homogenous analytical signals from ablation (Fig. 6). Therefore, these minerals were targeted for U–Pb dating using the laser ablation ICP-MS set-up described above for mineral trace element analysis. Analytes collected were ^{202}Hg, ^{204}Pb, ^{206}Pb, ^{207}Pb, ^{208}Pb, ^{232}Th, ^{235}U, and ^{238}U. The ICP-MS was tuned to ensure approximately equal sensitivity of U, Th, and Pb to minimise isotope fractionation due to matrix effects. An in-line Au trap was employed to minimise possible Hg contributions from the carrier gas. Full instrument set-up details are given in Tucker et al. (2013). Remaining fractionation and mass bias, as well as instrumental drift over time, was corrected by bracketing sets of 10 monazite or thorianite measurements by well-characterised primary calibration standards and secondary standards, as outlined below.

Monazite analyses were conducted using a 24-µm laser beam diameter with a 10-Hz pulse rate and laser energy density set to 3 J cm^{-2}. The Manangoutry (Paquette and Tiepolo 2007) and Namaqualand (Hokada and Motoyoshi 2006) monazites were analysed as the primary and secondary standards, respectively.

Matrix-matched standardisation is commonly employed for U–Pb dating by LA-ICP-MS primarily to account for downhole fractionation of Pb from U during ablation (Košler and Sylvester 2003). However, there are currently no widely available thorianite standards that can be used for U–Pb dating of thorianite. Therefore, we experimented with the ablation conditions to try and match trends in downhole fractionation of U and Pb in thorianite and zircon standards. We found that using a 24-µm beam diameter and 2-Hz repetition rate for the thorianite, and 32-µm beam size and 10-Hz repetition rate for the zircon standards gave very similar downhole U–Pb fractionation trends (Fig. 6). Using these analytical conditions, we achieved excellent signal intensities, and we are confident that we can eliminate potential problems associated with downhole U–Pb fractionation using non-matrix-matched standardisation in this case. Therefore, thorianite age dating was completed by bracketing thorianite analyses with two measurements of GJ1 zircon (primary calibration standard), and two Temora 2 and one FC1 zircon analyses (secondary checking standards).

Data reduction for all analyses was carried out using the Glitter software (Van Achterbergh et al. 2001). All time-resolved single-isotope signals from standards and samples were filtered for signal spikes or perturbations related to inclusions and fractures. Drift in instrumental measurements was corrected following the analysis of drift trends in the raw data using measured values for the primary standard (i.e. Manangoutry monazite or GJ1 zircon). Analyses of Temora 2 and FC1 zircons were used for the verification of GJ1 zircon following drift correction. The effect of common Pb is taken into account by the use of Tera–Wasserburg Concordia plots (Tera and Wasserburg 1972; Jackson et al. 2004), and weighted mean ^{206}Pb/^{238}U age calculations were carried out using Isoplot/Ex version 4.15 (Ludwig 2012). All errors were propagated at 2σ level.

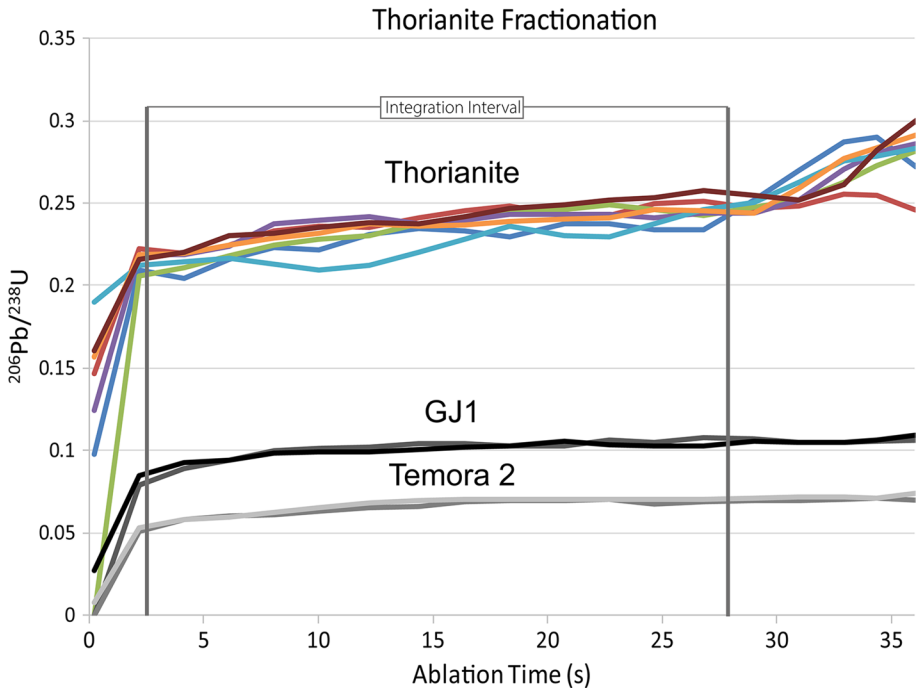

Fig. 6 Time-resolved LA-ICP-MS signal of ^{206}Pb/^{238}U isotope ratio for analyses of thorianite (2 s smooth) and GJ1 and Temora 2 zircon standards. Note that the slopes of the signals for the zircon and the thorianite analyses are similar across the integration interval used to calculate U–Pb ages, indicating that downhole fractionation effects are minimal

Analyses of the secondary standards serve as a check on the accuracy of our results. Analyses of the Namaqualand monazite gave a weighted mean age of 1031 ± 6 Ma, which is within error of the reference age of 1033 Ma (Hokada and Motoyoshi 2006). The Temora 2 and FC1 zircon secondary standards returned ages of 414.9 ± 6 Ma and 1103 ± 6 Ma, respectively, which is within the respective reference values of 416.8 ± 6 Ma (Black et al. 2004) and 1119 ± 16 Ma (Orihashi et al. 2008).

In situ Sm–Nd isotope microanalysis

In situ isotopic analyses of allanite and apatite were carried out at the AAC, JCU, using a ThermoScientific NEPTUNE MC-ICP-MS coupled to a Geolas 193-nm ArF excimer laser. The analytical set-up and procedures are outlined in detail in Hammerli et al. (2014). In situ laser ablation analyses were conducted on polished thin sections over 60 s with spot sizes of 16–90 μm, pulse rates of 4 Hz, and a laser energy density at the sample site of 3–6 J/cm^2. Interference and mass bias corrections were made according to the method of Fisher et al. (2011). The $^{147}Sm/^{144}Nd$ ratios were calibrated against a synthetic LREE-rich silicate glass ($^{147}Sm/^{144}Nd$ = 0.2451; (Fisher et al. 2011), which was routinely analysed throughout each session. Sample mineral $^{143}Nd/^{144}Nd$ ratios were further normalised to bracketing analyses of Nd-doped glass (JNdi-1, TIMS $^{143}Nd/^{144}Nd = 0.512098 \pm 13$, (Fisher et al. 2011).

We used three apatite grains as quality control material: Ap1 and Ap2 from Yang et al. (2008) and Durango Apatite. Our $^{143}Nd/^{144}Nd$ results for Ap1 and Ap2 of 0.511341 ± 23 (2SD) and 0.510999 ± 56 (2SD), respectively, agree well with those reported by from Yang et al. (2008); Ap1 = 0.511342 ± 31 (2SD) and Ap2 = 0.510977 ± 39 (2SD). Our analyses of Durango apatite gave $^{143}Nd/^{144}Nd$ values of 0.512467 ± 48 (2SD), which is in good agreement with the ratios acquired by LA-MC-ICP-MS reported in Foster and Vance (2006) (0.512469 ± 25) (2SD) and by Fisher et al. (2011) (0.512463 ± 48), and the TIMS value of 0.512489 ± 12 (Fisher et al. 2011). Our $^{143}Nd/^{144}Nd$ result for the LREE glass is 0.512096 ± 16 (2SD) which is indistinguishable from the value determined by TIMS (0.512098 ± 13, (Fisher et al. 2011). Sm–Nd isochrons were calculated from $^{147}Sm/^{144}Nd$ and $^{147}Sm/^{144}Nd$ ratios of coexisting allanite and apatite using Isoplot (Ludwig 2012).

Results

Bulk-rock analysis

In general, all rock types of Nolans Bore (ore and host rocks) have similar LREE-enriched REE patterns (Fig. 7a). The gneiss displays a negative europium anomaly, while the breccia types display minor negative europium anomalies. In general, the alteration zones have similar REE patterns and contents to the metasedimentary rocks, with the exception that more than half of the epidote alteration zone samples have distinct positive europium anomalies (Fig. 7b). Other epidote alteration samples have no or a slight negative europium anomaly.

Although the main REE-bearing mineral of the entire deposit is fluorapatite, both fluorapatite and allanite are important REE hosts in the central zone. Despite this, ore grade and REE patterns are similar across the deposit. Moreover, the P/REE Th/U, Th/P, and U/P ratios are similar for all ore types (Fig. 7c: Online Resource 1). Comparison of Fe and REEs throughout the deposit shows the Fe content increases from BX1–BX2: a feature that reflects the addition of allanite (Fig. 7d). However, if all components of allanite were being added to the system, this should have also increased the REE content, which is not observed. The Fe and REE contents then decrease from BX2 through BX3 and BX4-type breccia zones. This is due to the addition of amphibole and infill minerals that serve to dilute the concentration of Fe and REEs.

Mineral chemistry

Fluorapatite

We were unable to obtain accurate quantitative apatite data by WDS due to the effects of F diffusion by the electron beam (Goldoff et al. 2012). Nevertheless, qualitative EDS analysis reveals that all of the examined apatite is close to end-member fluorapatite, with a maximum measured Cl content of 0.16 wt%. There is, however, significant variation in the REE, Th, and U compositions of various apatite generations (Online Resource 1). There is a good correlation between the concentration of Si and REEs in apatite (Appendix 2), which indicates REEs are incorporated into apatite according to the exchange reaction, $Ca^{2+} + P^{5+} = REE^{3+} + Si^{4+}$ (Zirner et al. 2015).

BX1 fluorapatite contains around 5 wt% total rare earth element oxides (TREO), 1.0 wt% Th, 3000–5000 ppm Sr, and 500 ppm U. BX2 fluorapatite contains on average around 1 wt% TREO, 1000 ppm Sr, less than 200 ppm Th, and less than 20 ppm U. The inclusion-rich cores of fluorapatite from BX3 are of similar composition to BX2 apatite, whereas the inclusion-poor rims of BX3 fluorapatite (Figs. 4d, 8c) have significantly lower contents of REEs (~0.4 wt% TREO), Th (<50 ppm), and U (<8 ppm).

Apatite from four variants of BX1 ore all have similar LREE-enriched REE patterns (Fig. 9a). One minor exception is apatite from sample A27 that exhibits a positive cerium anomaly. The BX2 fluorapatite has similar HREE

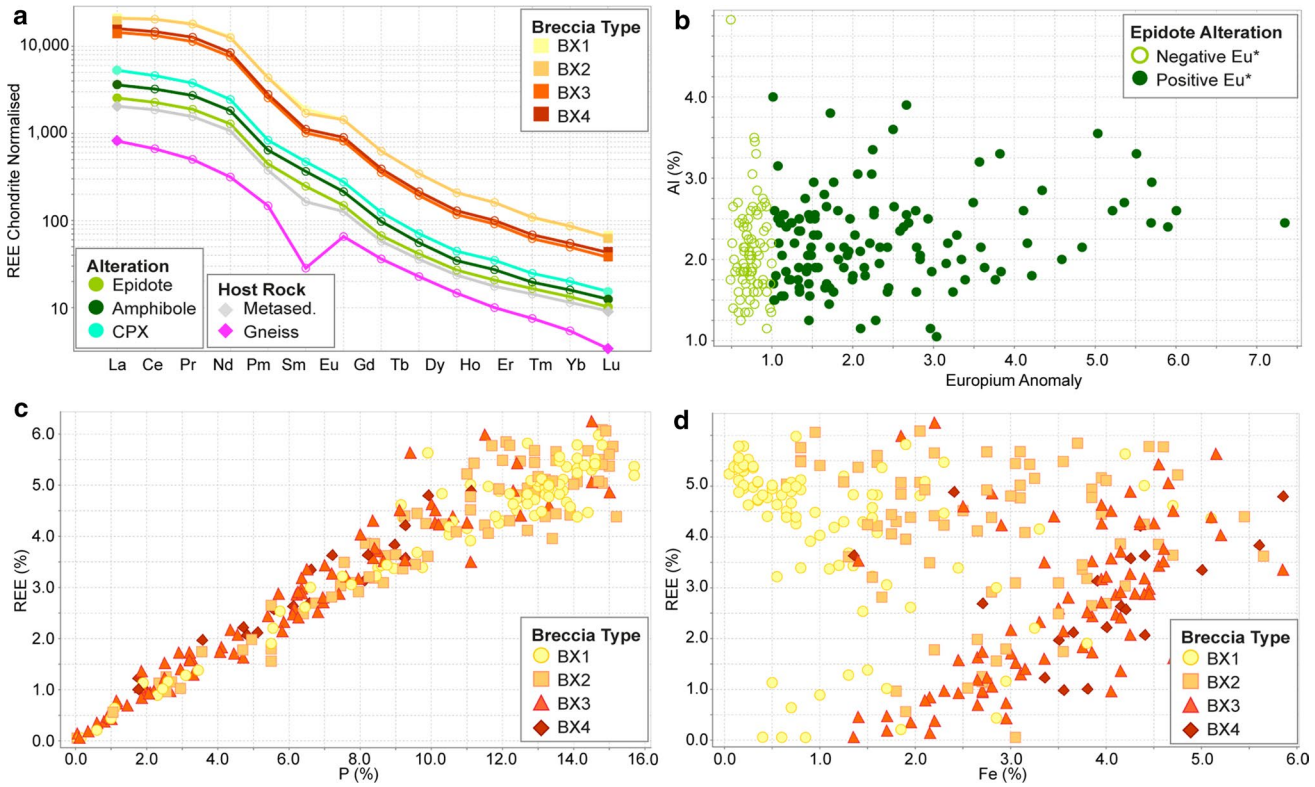

Fig. 7 Bulk-rock geochemical analysis. **a** Bulk-rock REE patterns of various ore types, alteration zones, and host rocks. REE values normalised using the chondritic values of Taylor and McLennan (1985). **b** Al content versus Eu anomaly (Eu*) of bulk-rock samples of the epidote alteration zones. Bulk-rock concentration of total rare earth elements. **c** versus P and **d** versus Fe between the ore types

contents to BX1 apatite, but is relatively depleted in LREE, and has a distinct negative Eu anomaly, giving an 'm-' shaped REE pattern (Fig. 9b). The allanite-inclusion-rich core zones of BX3 apatite are similar to BX2 apatite, while BX3 apatite rims have lower REE contents and a much smaller negative Eu anomaly (Fig. 9c).

Allanite/epidote

Allanite and epidote in the ore zones occurs both in early, coarse-grained allanite–carbonate veins that cut through the solid apatite veins, and as late-stage infill with amphibole. The compositional array follows a relatively simple substitution between epidote (sensu stricto) $Ca_2(Fe^{3+},Al)Al_2Si_3O_{12}(OH)$ and allanite $(Ca,Th,U,REE)_2(Fe^{2+},Al)_3Si_3O_{12}(OH)$, with no significant compositional gaps recognised. The early allanite in veins in BX1 has variable REE contents (7–25 wt% TREO; Fig. 10 and Appendix 3) and has lower Fe contents than allanite/epidote from the BX2 and BX3 ore. Epidote-group minerals from BX3 span a large compositional array, whereas BX2 contains mostly Fe-rich allanite compositions. In general, allanite with high REE contents are found as inclusions in fluorapatite, whereas epidote found as breccia infill tends to have lower and more variable REE contents. Epidote from the epidote–quartz–amphibole alteration zones has low REE contents (mostly <1 wt%) and is close to the epidote (s.s) end-member composition.

Concentrations of Th, U, and Sr can, respectively, reach up to 1 wt%, 6000 ppm, and 250 ppm, but the concentration of these elements tends to be negatively correlated with LREE content in allanite/REE-rich epidotes (Online Resource 2). Allanite from all breccia types has steep, LREE-enriched REE patterns, although BX1 allanite is depleted in HREEs compared to allanite from other breccia types (Fig. 9). BX2 and BX3 allanite (as both inclusions in apatite and as veins) also feature a prominent negative Eu anomaly. Epidote clasts in BX2 have relatively low REE contents and a positive Eu anomaly, and are likely representative of epidote from the epidote–quartz alteration zones. REE-epidote infill in BX3 (Fig. 9c) tends to have LREE-enriched patterns (albeit not as enriched as allanite) and may, or may not, have a Eu anomaly.

REE-Ca-carbonate, thorianite, and thorite

Based on WDS analyses, we identified several REE-bearing carbonate species, including hydroxyl-bastnaesite (Ce), hydroxyl-parisite (Nd), calcio-ancylite (Nd), and

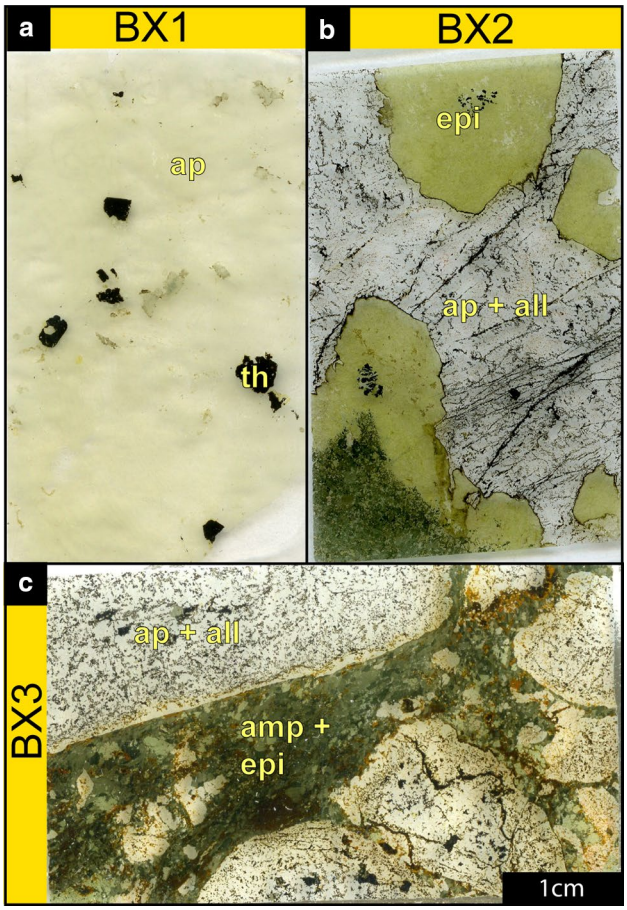

Fig. 8 Thin-section photographs of samples used for mineral analysis by LA-ICP-MS. **a** BX1-type apatite breccia with apatite clasts and ~5-mm thorianite inclusions; sample A5—NBDH1099 at 122.67 m. **b** BX2-type apatite breccia with clasts of the epidote within an apatite vein with thin allanite veinlets; sample A49—NBDH1099 at 163.05 m. **c** BX3-type apatite breccia with apatite clasts containing allanite inclusions. The infill is amphibole and REE epidote. The clasts of apatite have a rim of inclusion-free apatite; sample A8—NBDH1099 at 143.04 m. Abbreviation key: *all* allanite, *amp* amphibole, *ap* apatite, *epi* epidote, *th* thorianite

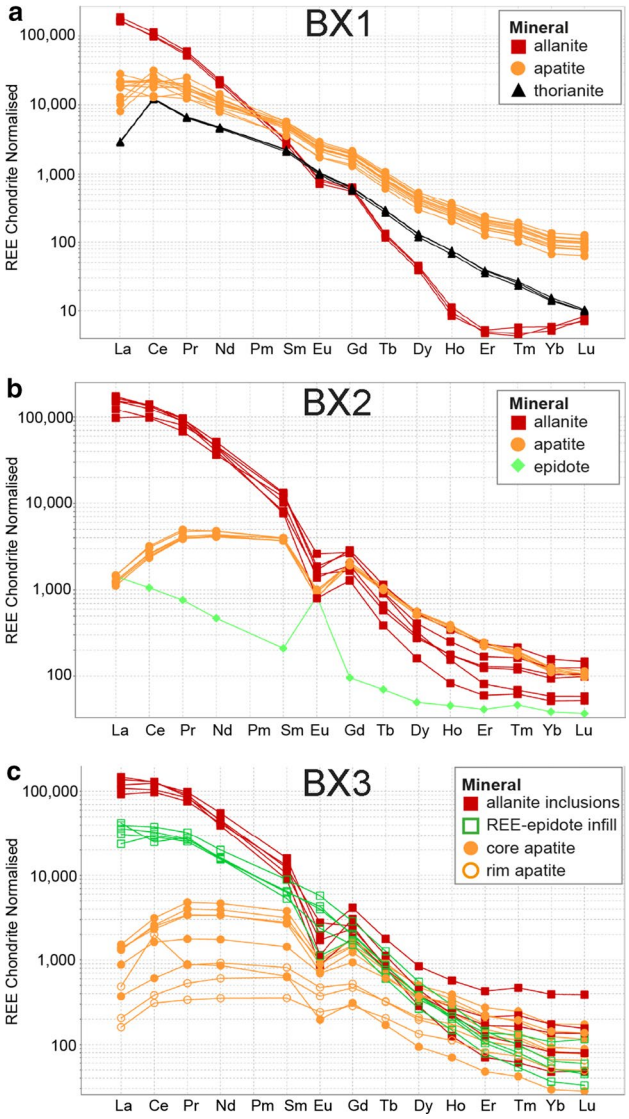

Fig. 9 Chondrite-normalised REE diagrams for minerals from the breccia types using chondrite values of Taylor and McLennan (1985). For images of the samples, refer to Fig. 8. **a** Allanite, apatite, and thorianite from multiple BX1 breccia samples. **b** Allanite, apatite, and epidote from BX2 breccia sample A49. **c** Allanite, apatite, and REE epidote from BX3 breccia sample A8

calcio-ancylite (Ce) (Fig. 11; Table 1). Fluorine was below detection limits in all analyses, and Sr contents range from <0.1 % (for bastnaesite) to over 4 wt% (for hydroxyl-parisite). Backscattered electron and X-ray mapping reveal that many grains feature spectacular zonation most clearly defined by the variations in Ce concentration, which ranges from 10 s of wt% Ce to <100 ppm Ce (Fig. 11 and Online Resource 2). REE patterns of all REE carbonates show extreme LREE enrichment (Fig. 11c) with LREEs in the wt% levels and HREEs (e.g. Yb) in the sub-ppm levels. The low-Ce zones are distinguished by a pronounced negative Ce anomaly (Fig. 11c).

Thorianite in BX1 veins is devoid of light elements, but is far from pure ThO_2; it contains ca. 7 wt% U, around 2 wt% TREO, significant amounts (~10 wt%) of radiogenic Pb, but low common ^{204}Pb (<20 ppm) (Online Resource 2). Thorianite has LREE-enriched REE patterns that plot at lower REE concentrations than either BX1 apatite or allanite (Fig. 9a). Thorianite also features a slight positive Ce anomaly.

Amphibole and pyroxene

The composition of amphibole varies little within and between samples. They are F-bearing actinolite of the approximate formula $Ca_2Mg_{3.7}Fe_{1.3}Si_8O_{22}[OH_{1.8}F_{0.2}]$ (Online Resource 2). Likewise, augitic pyroxene found as

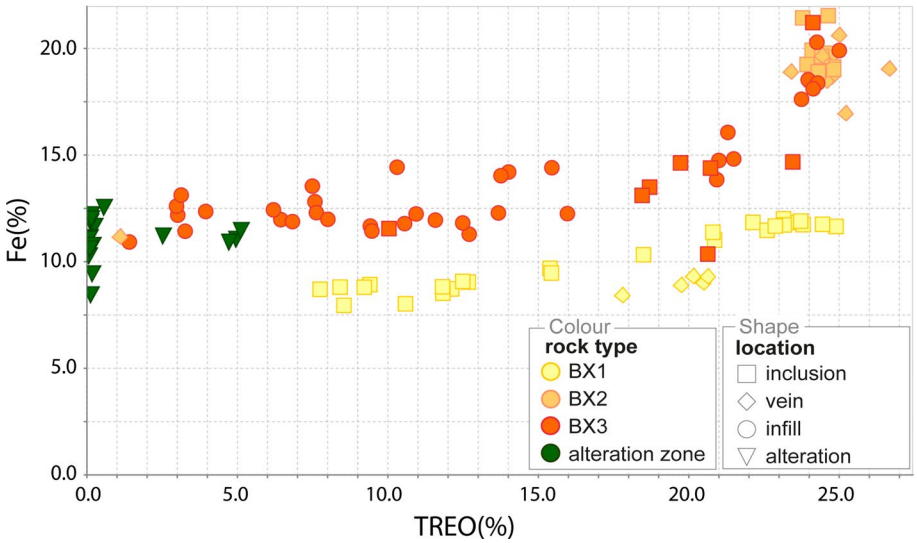

Fig. 10 Fe versus TREO content (wt%) of allanite/epidote from various breccia and alteration rock types. TREO is the sum of La, Ce, Pr, Nd, Sm, and Gd expressed as trivalent oxides. The *symbol shapes* indicate the textural setting of the allanite/epidote in the rock; 'inclusion' refers to allanite enclosed within apatite crystals; 'vein' represents small allanite-only veins cutting apatite grains; 'infill' constitutes minerals forming the infill of an apatite breccia, and; 'alteration' represents allanite/epidote in the alteration zones

clasts and as breccia infill shows little variation from the composition $CaMg_{0.75}Fe_{0.25}Si_2O_6$ (Online Resource 2). LA-ICP-MS analysis of these phases indicates that they contain low total REE contents of below 10 ppm.

Oxygen isotopes

Epidote, quartz, and amphibole separates from four samples from the alteration zone were analysed for oxygen isotopes to help constrain the temperature and composition of the hydrothermal fluid (Table 2). Epidote and quartz returned $\partial^{18}O$ (VSMOW) values of 3.9–4.8 ‰, and 7.0–7.5 per mil, respectively, while one sample of amphibole gave a value of 4.0 ‰. Applying the mineral–mineral and mineral–H_2O fractionation factors of Zheng (1993) to coexisting epidote and quartz pairs, fluid temperatures of between 470 and 620 °C were calculated. The $\partial^{18}O$ of the fluid at these conditions is calculated to be between 4.8 and 6.0 ‰ (Table 2).

Geochronology

U–Pb dating of BX1 thorianite

All thorianite analyses were made on a single large (~5 mm) thorianite grain from within BX1-type fluorapatite (Fig. 8). The thorianite grain appears to be internally homogenous and is largely free of inclusions, although it is enveloped by a thin (<100 µm) rim of thorite. All analysis produced smooth and homogeneous analytical signal, with no evident chemical zonation. The thorianite gives a relatively imprecise U–Pb concordia age of 1444 ± 80 Ma (Fig. 12a).

Sm–Nd isochron age of allanite, and apatite from BX2 and BX3

The high REE content and large difference in Sm–Nd of coexisting allanite and apatite in BX2 and BX3 (Fig. 9b, c) means that these mineral pairs are well suited for Sm–Nd isotope analysis to define isochron ages of ore mineral formation. The in situ technique employed here ensured that we were able to sample mineral domains that could be directly related through petrography. Apatite from BX2 samples returned $^{147}Sm/^{144}Nd$ and $^{143}Nd/^{144}Nd$ values of between 0.11 and 0.19, and 0.51115 and 0.5115, respectively, while $^{147}Sm/^{144}Nd$ and $^{143}Nd/^{144}Nd$ values of coexisting allanite are 0.03–0.05, and 0.51095 and 0.51105. The isochron produced from these data ($n = 29$) gives an age of 403 ± 15 Ma (MSWD = 1.15) and an initial $^{143}Nd/^{144}Nd$ value of 0.5109521 ± 89 (Fig. 12b).

Apatite and allanite from BX3 have isotopic compositions similar to the equivalent minerals from BX2 ($^{147}Sm/^{144}Nd$ and $^{143}Nd/^{144}Nd$ values of 0.12–0.18 and 0.51115–0.5115 and 0.03–0.07 and 0.5110–0.5112 for apatite and allanite, respectively). The isochron ($n = 16$) for BX3 returns a less precise age of 391 ± 32 Ma (MSWD = 0.87) and an initial $^{143}Nd/^{144}Nd$ value of 0.5109540 ± 180 (Fig. 12c).

U–Pb dating of BX4 monazite

BX4 breccias contain monazite as infill in the matrix (Fig. 4f) and in fractures in apatite; these monazites are interpreted to have formed during the last stage of mineral precipitation in these rocks. We have analysed monazite from two BX4 samples to determine U–Pb ages. Matrix

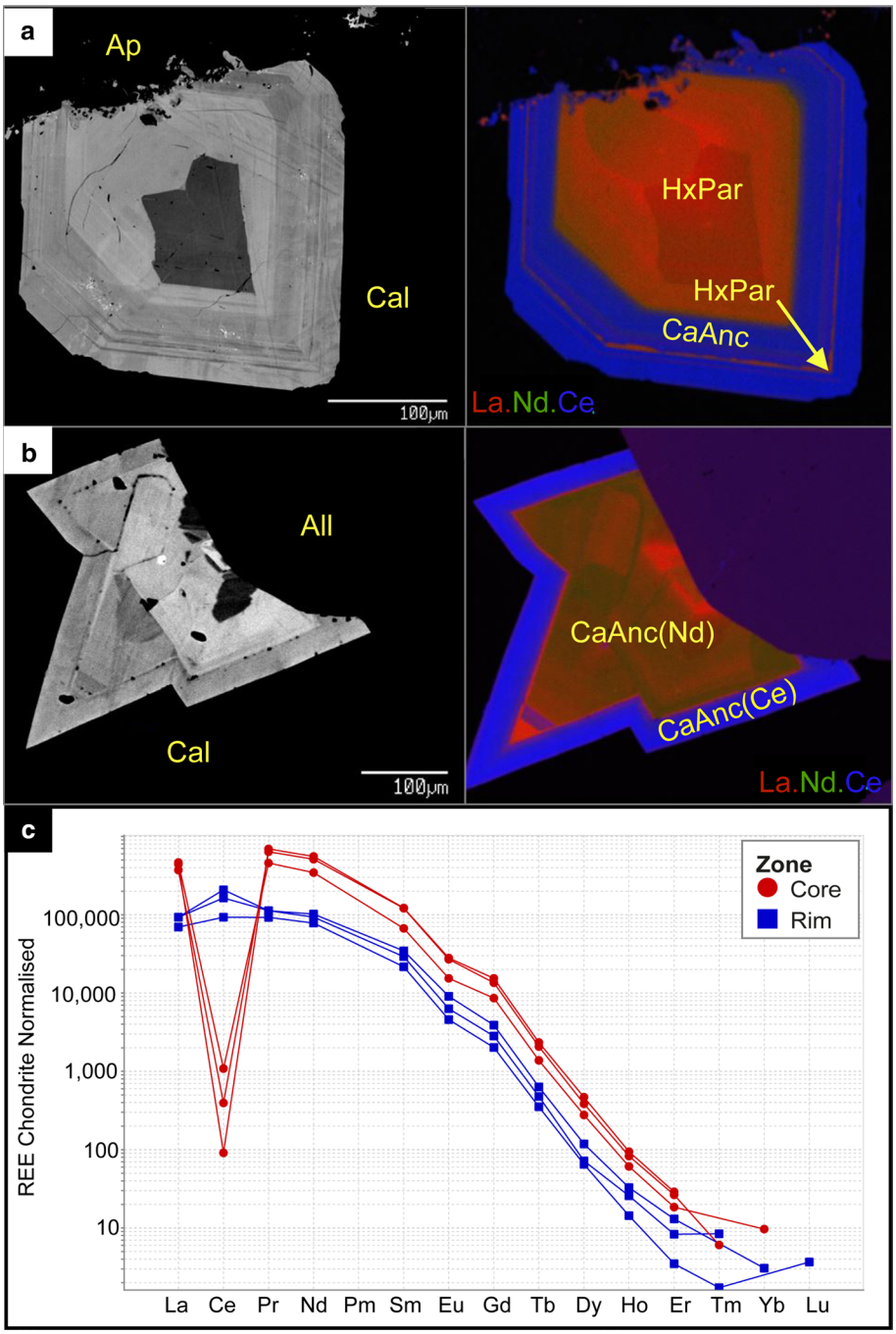

Fig. 11 Rare earth element zoned carbonate minerals. BSE image and composite REE element maps of zoned REE-Ca carbonate. The REE maps are a RGB composite image of separate La, Nd, and Ce X-ray maps. **a** REE-Ca-carbonate from breccia type BX4, located within calcite infill on the grain boundary of a coarse fluorapatite grain. The REE-carbonate grain contains a hydroxyl-parisite (Nd) core and calcio-ancylite (Ce) rim; sample A7-location; NBDH1099 at 125.97 m. **b** REE-Ca-carbonate in a BX1-type breccia located within calcite infill on the grain boundary of an allanite grain. The grain zones from Nd-rich calcio-ancylite to Ce-rich calcio-ancylite at the rim; sample A2, location NBRD173 at 109.49 m. **c** Chondrite-normalised (Taylor and McLennan 1985) REE patterns of core and rim zones of the calcio-ancylite crystal of BX1 sample A2. Abbreviation key: *all* allanite, *ap* apatite, *CaAnc* calcio-ancylite (with either Nd or Ce enrichment), cal calcite, *HxPar* hydroxyl-parisite

infill monazite from sample A6 (Fig. 4f) gave relatively homogeneous analytical signals with very low levels of ^{204}Pb. Eleven out of 17 spot analyses returned concordant ages that were used to calculate a U–Pb concordia age of 351.1 ± 4.6 Ma (MSWD = 0.38) (Fig. 12d). Analysis of small monazite grains in fractures in apatite from sample A23 gave poorer analytical signals due to short integration intervals and an inherited component of middle Proterozoic Pb. Eight out of 30 analyses that returned values on or close to U–Pb concordia gave an age of 344 ± 10 Ma (MSWD = 1.03).

Discussion

With a unique geological setting and mineralisation style, Nolans Bore is unlike any other orebody worldwide. The primary fluorapatite ore of the north and south-east zones

Table 1 Major element averages for REE-Ca-carbonate minerals in samples A7 and A2

Ore type	BX4								BX1					
Sample no.	A7								A2					
Mineral	Hydroxy-bastnäsite		Hydroxyl-parisite (Nd)		Calcio-ancylite (Ce)		Calcio-ancylite (Nd)		Hydroxyl-parisite (Nd)		Calcio-ancylite-(Nd)		Calcio-ancylite (Ce)	
Major elements	Average	1σ	Average	1σ	Average	1σ	Average	1σ	Average	1σ	Average	1σ	Average	1σ
CaO	0.32	0.01	8.87	0.15	6.88	0.14	6.69	0.07	9.25	0.27	6.11	0.44	6.33	0.30
SrO	0.03	0.04	3.69	0.78	0.96	0.53	1.48	0.09	2.34	0.69	1.60	0.43	2.37	0.22
La_2O_3	20.50	0.44	23.66	1.55	1.80	1.34	19.13	1.47	15.28	5.09	15.59	2.87	3.88	0.75
Ce_2O_3	36.50	0.26	0.00	0.00	52.95	2.70	0.00	0.00	0.05	0.10	0.06	0.08	46.14	3.19
Pr_2O_3	3.03	0.07	8.39	0.18	1.51	0.39	9.95	0.23	8.19	0.34	9.80	0.24	2.44	0.56
Nd_2O_3	8.28	0.10	29.71	2.55	8.70	1.33	37.31	1.86	36.43	3.81	40.93	2.26	12.65	1.93
F	0.00	0.00	0.00	0.00	0.00	0.00	0.00	0.00	0.00	0.00	0.00	0.00	0.00	0.00
H_2O (calc)	3.82	0.05	3.39	0.01	3.56	0.03	3.60	0.02	3.28	0.08	3.55	0.04	3.58	0.02
CO_2 (calc)	27.99	0.38	24.85	0.08	23.17	0.20	23.46	0.15	24.02	0.59	23.12	0.29	23.30	0.14
Total	101.20	1.37	102.55	0.48	99.53	0.92	101.63	0.78	98.83	2.51	100.76	1.37	100.67	0.74
Cations based on three oxygen														
Ca	0.03	0.00	0.84	0.01	0.93	0.02	0.90	0.01	0.91	0.03	0.83	0.06	0.85	0.04
Sr	0.00	0.00	0.19	0.04	0.07	0.04	0.11	0.01	0.12	0.03	0.12	0.03	0.17	0.02
La	0.59	0.00	0.77	0.05	0.08	0.06	0.88	0.07	0.51	0.16	0.73	0.13	0.18	0.03
Ce	1.05	0.01	0.00	0.00	2.45	0.14	0.00	0.00	0.00	0.00	0.00	0.00	2.12	0.15
Pr	0.09	0.00	0.27	0.01	0.07	0.02	0.45	0.01	0.27	0.02	0.45	0.01	0.11	0.03
Nd	0.23	0.00	0.94	0.08	0.39	0.06	1.66	0.07	1.19	0.14	1.85	0.11	0.57	0.09
Sm*	0.02	0.00	0.00	0.00	0.00	0.00	0.00	0.00	0.00	0.00	0.00	0.00	0.00	0.00
Cation total	2.01	0.00	3.01	0.02	4.00	0.01	4.00	0.00	3.01	0.01	3.98	0.02	4.01	0.01
REEs	1.98	0.00	1.98	0.03	3.00	0.01	3.00	0.01	1.98	0.02	3.04	0.03	2.98	0.02
Ca + Sr	0.03	0.00	1.03	0.05	1.00	0.02	1.00	0.01	1.03	0.03	0.95	0.05	1.02	0.03
Formula	(Ce, La) CO_3(OH,F)		$Ca(Nd,La)_2$ $(CO_3)_3(OH)_2$		(Ca,Sr)(Ce,Nd) $(CO_3)_2$ $(OH)\cdot(H_2O)$		(Ca,Sr)(Nd,La) $(CO_3)_2$ $(OH)\cdot(H_2O)$		$Ca(Nd,La)_2$ $(CO_3)_3(OH)_2$		(Ca,Sr)(Nd,La) $(CO_3)_2$ $(OH)\cdot(H_2O)$		(Ca,Sr)(Ce,Nd) $(CO_3)_2$ $(OH)\cdot(H_2O)$	

H_2O and CO_2 contents calculated based on the consideration of stoichiometry and major element totals

* Sm calculated based on Nd content and LA-ICP-MS data

(Fig. 1) cuts ancient granulite-grade rocks with limited resulting host rock alteration. The relatively simple mineralogy and alteration features of this primary vein type of mineralisation provide relatively few geological tools to investigate the origin of the REE mineralisation. By contrast, the central zone is the most complex section of the deposit and therefore has the potential to reveal much more about the evolution of the deposit. In order to decipher this information, the structural (i.e. brecciation stages), petrological, and geochronological evolution of the deposit needs first to be defined. We then use this information to evaluate REE mobility during hydrothermal alteration, the nature and source of the hydrothermal fluids involved, and the timing of alteration events. Finally, we discuss the implications of our findings for the geological history of the region, and the potential of applying our methodologies to understanding the geochemical and temporal evolution of other ore systems.

Paragenesis and evolution of the central zone

The central zone is a mineralogical medley produced from a series of events beginning with the formation of massive fluorapatite veins into the granulite-grade host rocks, followed by numerous episodes of brecciation and recrystallisation of the ore. The reason for the higher level of structural and mineralogical complexity in the central zone in comparison with other ore zones of the deposit is due to (1) ore formation along the contact between metagranitic and metasedimentary rocks, which have a large rheological contrast and hence become a focus of strain during deformation events; (2) the north–south orientation of the central zone, which is thought to have been favourable for reactivation during deformation events subsequent to primary ore formation. The north and south-east ore zones largely preserve the primary fluorapatite vein arrays that

Table 2 Oxygen isotope composition of silicate minerals from the alteration zones and calculated temperatures and fluid compositions

Sample number	Mineral	$\delta^{18}O$ mineral	Temp. °C (ep-qtz pairs)	$\delta^{18}O$ fluid
NBDH1095 70.6	Epidote	3.9	470	4.8
NBDH1095 70.6	Quartz	7.5		
NBDH1095 109.6	Epidote	4.3	615	5.7
NBDH1095 109.6	Quartz	7.0		
NBDH1095 61.3	Epidote	4.3	615	5.7
NBDH1095 61.3	Quartz	7.0		
NBRD 104 123.7	Epidote	4.8		6.0*
NBDH 068 49.25	Hornblende	4.0		5.8*
Lander rock beds[#]				13.4–6.7
Unsheared granites[#]				7.0–9.3

Uncertainty of isotope measurements is 0.1 ‰. Temperatures and fluid compositions were calculated using the epidote–quartz–H_2O fractionation factors of Zheng (1993)

* Fluid composition calculated assuming a temperature of 550 °C

[#] Data from Cartwright et al. (2000)

have a general east–north-east trend and are hosted almost entirely in highly competent metagranitic gneisses. We suggest these conditions effectively shielded the ore from subsequent regional deformation events. Nevertheless, even here there is some evidence for post-formation isotopic resetting of the ore (Maas et al. 2009). Huston et al. (2015) suggested that the high levels of radiogenic heat produced by the elevated thorium and uranium in the veins, as well as the host rocks, could have sustained relatively high temperatures in the deposit (>300 °C) for a period of nearly 1 billion years after vein formation. The prolonged high temperatures in the deposit may also have been favourable to reactivation and reworking of ore in the central zone.

A mineral paragenesis table was formulated based on textural relationships at the core scale and microscale, coupled with geochemical evidence such as trace element distribution between coexisting minerals and the available geochronological data (Fig. 13). Huston et al. (2015) suggest that the primary fluorapatite veins of the north zone precipitated at ca. 1525 Ma from fluids evolved from deep-seated alkali intrusions that were generated from melting of an enriched lithospheric mantle source. We expect that such primary fluorapatite veins also formed the precursor ore type in the central zone. The mineralogical, geochemical, and textural evolution of subsequent ore types (BX1–BX4) is outlined below.

BX1

The BX1 apatite has undergone extensive alteration, as evident from complex zonation textures in BSE imaging (e.g. Fig. 4a) and abundant microscale (<10 µm) inclusions of minerals such as monazite and thorite (Fig. 4a). Similar features have been described from other natural metasomatic apatites (Engvik et al. 2009) and experimentally altered apatites (Harlov and Förster 2004; Harlov et al. 2005), and are regarded to be the production of hydrothermal dissolution/reprecipitation processes (Putnis 2009). Nevertheless, the recrystallisation is not expected to have induced significant repartitioning of REEs, as all ore minerals have similar LREE-enriched REE patterns (Fig. 9a). Fluorapatite contains up to several wt% of REEs and therefore is the main ore mineral.

Thorianite interpreted to be part of the BX1 paragenesis yielded an U–Pb age of 1444 ± 80 Ma, which is just within uncertainty of the determined age of the primary fluorapatite veins from the north zone (ca.1525 Ma; Huston et al. 2015). However, we do not assign these two determined ages to a single event, as we interpret BX1 formation to be a later alteration of the solid apatite veins. Instead, we correlate the ca. 1440 Ma age of BX1 to the large regional event known as the Redbank Shear Zone. The Redbank Shear Zone (1500–1400 Ma) caused massive shearing and localised alteration by hot (~650–550 °C) hydrous fluids in the southern province of the Arunta Region (Shaw and Black 1991; Hand and Sandiford 1999). Alteration caused by this event may be more pervasive than commonly recognised, as there is also evidence of isotopic disturbance of minerals within Nolans Bore north zone (Maas et al. 2009) and the region (Buick and Cartwright 1996) at this time.

BX2 and BX3

The BX2 and BX3 breccias represent the bulk of the ore in the central zone, and are interpreted to be the products of subsequent brecciation and alteration of the ore zones. Both brecciation events involve introduction of significant calc-silicate (+Fe +Mg) components to form allanite, amphibole, clinopyroxene, and/or epidote. Nevertheless, the REE grade of these breccia zones (particularly BX2) is comparable to the BX1 type and solid fluorapatite veins (Fig. 7) due to the formation of allanite and trace REE carbonates. Moreover, the P/REE ratio of all ore zones remains relatively constant, which suggests that the newly formed allanite and REE carbonate did not introduce additional REEs, but rather recycled REEs (as well as U, Th, and Sr)

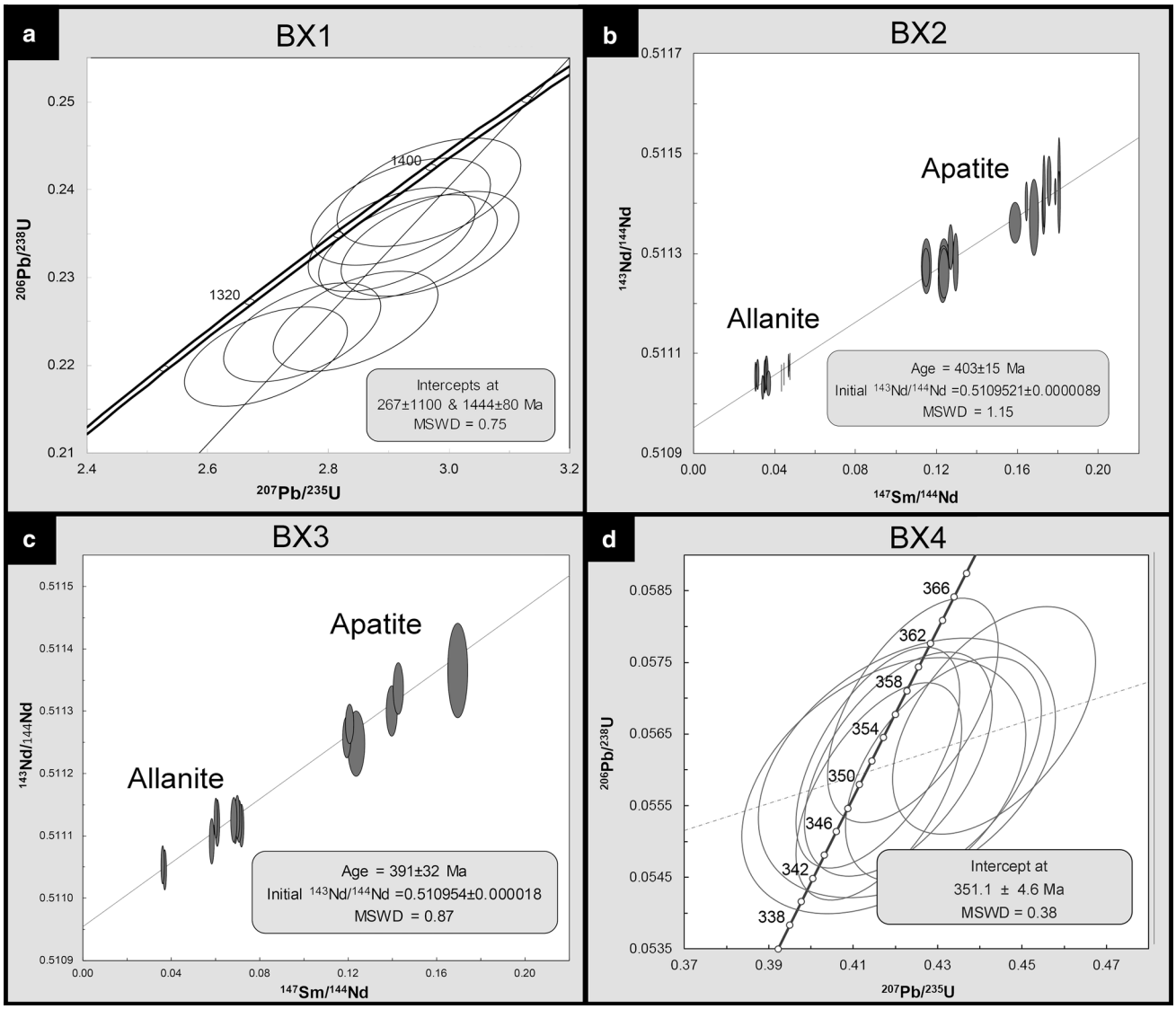

Fig. 12 U–Pb and Sm–Nd isochrons of ore breccia types. **a** U–Pb concordia diagram with analyses of thorianite from BX1 breccia (sample A5; Fig. 8a). **b** Sm–Nd isochron of coexisting allanite and apatite from BX2-type breccia. **c** Sm–Nd isochron of coexisting allanite and apatite from BX3-type breccia. **d** U–Pb concordia diagram with analyses of late monazite infill in the BX4 (sample A6; see Fig. 4f). Data-point error ellipses are 2σ

Fig. 13 Mineral paragenesis chart for the ore types of the central zone of Nolans Bore. *Age of allanite from the north zone from Huston et al. (2015)

Stage / Mineralogy	Original Veining ~1520 Ma*	BX1 ~1440 Ma	BX2 ~400 Ma	BX3 ~400 Ma	BX4 ~350 Ma
REE-Apatite	—				
Thorianite		—			
Exsolution Minerals		—			
REE-Carbonates		- - -			- - -
Calcite		- - -			
Apatite			—	—	
Allanite			—	—	
Epidote			—		
Amphibole				—	
Monazite					- - -

from the original fluorapatite, according to the simplified reaction (1):

$$\text{REE-rich fluorapatite} + \text{Ca, Si, Fe (fluid)} \rightarrow \text{REE-poor fluorapatite} + \text{allanite} \quad (1)$$

This reaction is supported by the REE compositions of ore minerals, as the BX1-type fluorapatite contains higher LREE contents than the fluorapatite from the BX2-BX3 breccias that co-precipitated with LREE-rich phase allanite, REE epidote, and/or REE carbonate (Fig. 9). This effective redistribution of REEs indicates these elements did not mobilised any significant distance (i.e. sub-cm scale) during alteration and brecciation of the central zone ore. This result is consistent with numerous other studies that have demonstrated limited REE mobility during reaction of phosphate minerals with hydrothermal fluids (e.g. Harlov and Förster 2004) or melts (Wolf and London 1995), and also validates the use of the Sm–Nd isotope composition of REE mineral pairs to construct meaningful isochrons for the timing of brecciation (Fig. 12).

The Sm–Nd isochrons calculated from texturally cogenetic allanite and apatite from both BX2 and BX3 give ages around 400 Ma. Our in situ microanalysis technique combined with the well-constrained paragenetic relationships (i.e. reaction 1) means that we have great confidence that these isochrons precisely date the brecciation events. The similarity in ages and mineral geochemistry (Fig. 9), as well as the textural continuity between these breccia styles, lends support to the idea that these two breccia types may represent products of the same alteration event. The age falls within the time window of the Alice Springs Orogeny (450–300 Ma; Raimondo et al. 2011), which extends the known geological record of this event in the region.

Alteration zone

The extensive (>50 m thick) epidote–quartz (± amphibole) alteration zone associated with central zone is not observed in other ore zones of Nolans Bore where the alteration envelope around the ore veins tends to be less than 1 m thick. The alteration zone of the central zone is developed within metasedimentary host rocks (Fig. 2), which may have been more permeable to alteration fluids than the granitic gneiss. These alteration zones have REE contents that are intermediate between the ore and unaltered host rocks (Fig. 7a). Nevertheless, we can confidently link the development of the alteration zone to the formation of the BX2 and BX3 breccias. Firstly, BX2 and BX3 ore minerals feature negative Eu anomalies, which are not observed in the precursor BX1 minerals (Fig. 9). The Eu deficit in BX2 and BX3 can be explained by preferential uptake of Eu (as Eu^{2+}) into cogenetic epidote in the alteration zone (Fig. 7b). Furthermore, a qualitative age of approximately 400 Ma from titanite in the epidote–quartz alteration zone also links the formation of the extensive alteration envelope with the formation of the BX2 and BX3 breccias. Confirmation of this genetic link is important, as minerals of the alteration zone are used to determine fluid compositions and conditions of hydrothermal alteration, as outlined below.

BX4

Although the BX4 breccias are relatively rare, they represent the most complex ore type of the central zone and provide evidence of yet another episode of alteration at Nolans Bore. BX3 and BX4 breccias share many geochemical and mineralogical characteristics, but BX4 is more complex, being clast-supported, chaotic, rubble breccias that also contain minor late infill of monazite, phlogopite, calcite, and REE carbonate (Fig. 4e, f). The infill assemblage of monazite, calcite plus phlogopite, is explained by the simplified reaction (2) below:

$$\text{allanite/REE-rich fluorapatite} + K^+(\text{fluid}) + CO_2(\text{fluid}) \rightarrow \text{monazite} + \text{calcite} + \text{phlogopite} \quad (2)$$

We interpret the U–Pb age of ca. 350 Ma from this late monazite infill to represent the timing of BX4 brecciation. This age is significantly younger than the ages of BX2 and BX3 breccias, but still corresponds with the timing of the Alice Springs Orogeny and in particular the timing of mylonitic deformation for the north zone of Nolans Bore, as determined from Ar–Ar geochronology of muscovite (Huston et al. 2015). The implication here is that the Nolans Bore deposit was affected by at least two discrete alteration events during the Alice Springs Orogeny.

Source and composition of hydrothermal fluids

The source of the primary fluorapatite veins has been studied in detail by Huston et al. (2011, 2015), and so is only briefly reviewed here. The primary mineralisation is suggested to have formed at ca. 1525 Ma from halogen- and phosphate-rich alkali fluids that originated from mantle-derived alkaline magmatism. An alkaline fluid composition is also consistent with the ore mineral assemblage dominated by REE fluorapatite, with little to no allanite or monazite (Krenn et al. 2012).

BX1 fluids

Although we have little information to evaluate the source of fluids for the BX1 breccias, we can use phase petrology and mineral geochemistry to infer aspects of the altering

fluid composition. The brecciation and dissolution/reprecipitation of fluorapatite veins associated with the BX1 event produced an assemblage of calcite and REE carbonates, fluorapatite, thorianite, and minor monazite and allanite. Minerals of this assemblage were produced by hydrothermal experiments on REE minerals at mid-crustal pressures (0.45–1.0 GPa) and temperatures (450–900 °C) by Harlov and Förster (2004) and Budzyń et al. (2011). Applying these authors' results, we infer that BX1 alteration fluids were relatively oxidising (to stabilise thorianite) hydrous fluids with a minor $CaCO_3$ component (to form carbonates, plus minor monazite and allanite). Extensive recrystallisation of fluorapatite via dissolution/reprecipitation processes indicates that the fluid phase was relatively acidic (Ayers and Watson 1991; Harlov et al. 2005). The hydrous and oxidised nature of the fluid can also explain the hydroxyl composition and Ce-deficient core zones of REE-carbonate minerals (Fig. 11b, c), as under oxidising conditions Ce manifests as Ce^{4+}, which is excluded from the carbonate structure. The carbonate rim zones do not feature negative Ce anomalies, which indicates that redox conditions were variable during carbonate precipitation. These fluctuations may be due to localised fluid rock reaction effects or may be indicative of fluid mixing during alteration.

BX2 and BX3 fluids

The most significant event to affect the central zone was the hydrothermal alteration and brecciation that produced the BX2 and BX3 breccias and broad epidote–quartz alteration zones at ca. 400 Ma. The breccia zones are distinguished by the extensive development of calc-silicate minerals, including allanite and REE epidote, without monazite, which is consistent with alteration by Ca-bearing, low-alkali hydrous fluids (Harlov and Förster 2004; Budzyń et al. 2011). Again, acidic fluids are invoked to explain the extensive fluorapatite dissolution to allow REEs to form allanite and/or REE epidote according to reaction 1. In this case, however, the fluids were relatively reduced, as the development of prominent Eu anomalies in the ore minerals and epidote alteration zones (Figs. 7b, 9b, c) suggests that Eu existed in the reduced Eu^{2+} form (which is expected to substitute readily for Ca^{2+} in epidote).

Both epidote and actinolitic amphibole that are widely developed in the alteration zone around the ore are hydroxyl-rich, with minor F contents and low Cl contents, which suggests that the alteration fluids were not Cl-rich. The F component is likely to be a remnant of dissolution of the original fluorapatite veins. The low halogen content of these infiltrating fluids would also have made them a poor carrier of REE (Williams-Jones et al. 2012), which, together with the low REE content of these minerals, further supports conservative REE behaviour during alteration.

The presence of actinolite together with diposide as dominant alteration minerals can also help to constrain the temperature of alteration. Using the amphibole + clinopyoxene stability relations of Hellner and Schürmann (1966) and Lledo and Jenkins (2008), we can limit hydrothermal alteration temperatures to between 450 and 800 °C, at relevant pressure conditions (>0.1–0.3 GPa) at Nolans Bore at this time. Tighter constraints on alteration conditions can be gained from the oxygen isotope composition of epidote and quartz from the alteration zones, assuming equilibrium between these two minerals. Using the isotope fractionation factors of Zheng (1993), our data are used to infer alteration temperatures of between 470 and 615 °C (Table 2), which agree well with the broad constraints from amphibole stability relations.

Our geochronology data clearly place this alteration event in the Alice Springs Orogeny. Thermobarometry studies have estimated alteration associated with shear zone activation, during the Alice Springs Orogeny, to be approximately 530 °C and 0.4–0.5 GPa (Raimondo et al. 2011), which corresponds well with our temperature estimates for the alteration of the central zone at ca. 400 Ma. The calculated isotopic composition of the alteration zone fluids (4.8–6.0 ‰; Table 2) is below the values of crustal rocks of the Reynolds Range (Cartwright et al. 2000), but is consistent with a mixed meteoric fluid/metamorphic fluid source, as has been proposed to explain similar isotopic signatures for Alice Springs shear zone fluids (Anderson et al. 2013, 1999; Cartwright et al. 2000; Read and Cartwright 2000; Raimondo et al. 2011).

BX4 fluids

The BX4 breccias were formed during exhumation at the waning stages of the Alice Springs Orogeny (Raimondo et al. 2011). There is little infill associated with these breccias, so evidence of the fluid composition is limited. Nevertheless, the infill assemblage of monazite, carbonates, and phlogopite formed via reaction 2 is consistent with formation from low Ca, CO_2-bearing, potassic fluids (Harlov and Förster 2004; Budzyń et al. 2011). These geochemical attributes are consistent with gains in K and losses in Ca documented in other Alice Springs shear zones (Raimondo et al. 2011). As in BX1, REE-carbonate grains are commonly zoned from Ce-deficient cores (Fig. 11a) to Ce-rich rims, which indicate that redox conditions (at least locally) varied between relatively oxidised to relatively reduced conditions.

In summary, the central zone at Nolans Bore has developed through at least three alteration and brecciation events, each involving hydrothermal fluid with distinct

compositions. The BX1 breccias were formed by acidic, oxidised, hydrous fluids, whereas the BX2 and BX3 ores formed in response to widespread alteration and brecciation by Ca-rich, alkali-poor, reduced fluids. The final alteration stage involved influx of relatively oxidised K-rich, Ca-poor fluids to form the BX4 breccias. In general, this geological history conforms with previous interpretations of the structural and hydrothermal evolution of the southern Reynolds Range (e.g. Collins and Shaw 1995 and Raimondo et al. 2011), but our data may also offer additional information that can aid in understanding the geological development of the region, as we discuss below.

Implications for regional geological histories

We have shown that the central zone of Nolans Bore preserves evidence of the major deformation episode to affect the Reynolds Range, since primary ore formation in the middle Proterozoic. The BX1 event can be correlated to the Redbank Shear Event, while BX2–BX4 are related to the Alice Springs Orogeny. Specifically, the BX2 and BX3 events may correspond to the compressional 370- to 390-Ma Pertnjara-Brewers Movement recognised across the region (Buick et al. 2008; McLaren et al. 2009), while the 350-Ma BX4 breccia may have formed during exhumation at the waning stages of the Alice Springs Orogeny.

Understanding the regional geological context of the genesis of ore bodies is essential for further mineral exploration targeting. However, it is often difficult to obtain meaningful geochemical, geochronological, and petrological information from the mineral assemblages that define many sulphide ore bodies. In contrast, numerously deformed and reworked REE orebodies, such as the central zone of Nolans Bore, may be exceptional archives of the regional geological history, as they contain REE- and actinide-rich mineral parageneses that are excellent geochronological and geochemical recorders of geological events. We have shown that microscale in situ analysis of REE minerals, (using, e.g. LA-MC-ICP-MS), coupled with contextualised mineral paragenesis studies can be very effective in unravelling the complex geological history of hydrothermal orebodies. In this paper, we record a history of brecciation in the central zone of Nolans Bore that extends over 1 billion years. As discussed above, competency contrasts between the apatite-rich ore and granulite-grade host rocks, and an elevated local geothermal gradient due to radiogenic heating (see Huston et al. 2015), would have favoured repeated brecciation of this zone during regional-scale deformation events. We expect that similar techniques could be used very effectively in other REE orebodies (e.g. Bayan Obo, Smith et al. 2000; Hoidas Lake, Pandur et al. 2014) to help unravel the origin and history of these ore systems and their geological setting.

Conclusions

We combine detailed microtextural analysis, mineral major and trace element geochemistry, mineral O isotope analysis, and microscale U–Pb and Sm–Nd geochronology to investigate the geological history of the central zone of the Nolans Bore REE deposit. We demonstrate that alteration of primary REE-rich fluorapatite ore resulted in effective redistribution of REEs into newly formed allanite, REE-poor apatite, and REE carbonate (±monazite, ±thorianite) during repeated episodes of brecciation and hydrothermal alteration. We document three deformation/brecciation events to affect the central zone. All three alteration events involved basinal/metamorphic fluids and/or meteoric fluids.

- BX1 breccia formed at ca. 1450 Ma during the Redbank Shear Event. The infiltration fluids were hydrous, oxidising, and acidic in nature
- BX2 and BX3 breccias and associated epidote–quartz-rich alteration zone formed at ca. 400 Ma under probably compressional regime during the Alice Springs Orogeny. Infiltrating fluids were low alkali and Ca-rich, but relatively reducing.
- BX4 breccias developed at 350 Ma during exhumation at the waning stages of the Alice Springs Orogeny. In this case, that alteration fluids were low Ca, K-rich, oxidising, carbonate-bearing hydrous fluids.

Acknowledgments This research was undertaken in part as an honours research project at James Cook University. The work was funded through an ARC Future Fellowship (FT 120100198) to Spandler and was supported by Arafura Resources Ltd, who provided some research funding and access to the Nolans Bore core and assay database. The Advanced Analytical Centre (AAC) staff at James Cook University helped immensely with the data collection and analytical techniques. This contribution has also benefitted from editorial handling of Chris Ballhaus and the reviews of Vadim Kamenetsky and an anonymous reviewer.

References

Anderson JR, Kelsey D, Hand M, Collins WJ (2013) Conductively driven, high-thermal gradient metamorphism in the Anmatjira Range, Arunta region, central Australia. J Metamorph Geol 31:1003–1026

Black LP et al (2004) Improved 206Pb/238U microprobe geochronology by the monitoring of a trace-element-related matrix effect; SHRIMP, ID–TIMS, ELA–ICP–MS and oxygen isotope documentation for a series of zircon standards. Chem Geol 205:115–140. doi:10.1016/j.chemgeo.2004.01.003

Budzyń B, Harlov DE, Williams ML, Jercinovic MJ (2011) Experimental determination of stability relations between monazite, fluorapatite, allanite, and REE-epidote as a function of pressure, temperature, and fluid composition. Am Miner 96:1547–1567

Buick IS, Cartwright I (1996) Fluid-rock interaction during low-pressure polymetamorphism of the Reynolds Range Group, Central Australia. J Petrol 37:1097–1124

Buick IS, Storkey A, Williams IS (2008) Timing relationships between pegmatite emplacement, metamorphism and deformation during the intra-plate Alice Springs Orogeny, central Australia. J Metamorph Geol 26:915–936

Cartwright I, Buick IS (1999) The flow of surface-derived fluids through Alice Springs age middle-crustal ductile shear zones, Reynolds Range, central Australia. J Metamorph Geol 17:397–414. doi:10.1046/j.1525-1314.1999.00205.x

Cartwright I, Buick I, Vry J (2000) The time-integrated history of crustal fluid flow: Reynolds Range, central Australia. J Geochem Explor 69–70:353–357. doi:10.1016/S0375-6742(00)00091-1

Chakhmouradian AR, Zaitsev AN (2012) Rare earth mineralization in igneous rocks: sources and processes. Elements 8:347–353. doi:10.2113/gselements.8.5.347

Claoué-Long JC, Hoatson DM (2005) Proterozoic mafic–ultramafic intrusions in the Arunta Region, central Australia: part 2: event chronology and regional correlations. Precambr Res 142:134–158. doi:10.1016/j.precamres.2005.08.006

Claoué-Long J, Edgoose C, Worden K (2008) A correlation of Aileron Province stratigraphy in central Australia. Precambr Res 166:230–245. doi:10.1016/j.precamres.2007.06.022

Collins WJ, Shaw RD (1995) Geochronological constraints on orogenic events in the Arunta Inlier: a review. Precambr Res 71:315–346. doi:10.1016/0301-9268(94)00067-2

Collins WJ, Teyssier C (1989) Crustal scale ductile fault systems in the Arunta Inlier, central Australia. Tectonophysics 158:49–66. doi:10.1016/0040-1951(89)90314-4

Collins WJ, Williams IS (1995) SHRIMP ionprobe dating of short-lived Proterozoic tectonic cycles in the northern Arunta Inlier, central Australia. Precambr Res 71:69–89. doi:10.1016/0301-9268(94)00056-W

Dirks PHGM (1990) Intertidal and subtidal sedimentation during a mid-Proterozoic marine transgression, reynolds range group, Arunta block, central Australia. Aust J Earth Sci 37:409–422. doi:10.1080/08120099008727941

Dirks PHGM, Hand M, Powell R (1991) The P–T-deformation path for a mid-Proterozoic, low-pressure terrane: the Reynolds Range, central Australia. J Metamorph Geol 9:641–661. doi:10.1111/j.1525-1314.1991.tb00553.x

Engvik AK, Golla-Schindler U, Berndt J, Austrheim H, Putnis A (2009) Intragranular replacement of chlorapatite by hydroxy-fluor-apatite during metasomatism. Lithos 112:236–264

Fisher CM, McFarlane CRM, Hanchar JM, Schmitz MD, Sylvester PJ, Lam R, Longerich HP (2011) Sm–Nd isotope systematics by laser ablation-multicollector-inductively coupled plasma mass spectrometry: Methods and potential natural and synthetic reference materials. Chem Geol 284:1–20

Foster GL, Vance D (2006) In situ Nd isotopic analysis of geological materials by laser ablation MC-ICP-MS. J Anal At Spectrom 21:288–296

Goldoff B, Webster JD, Harlov DE (2012) Characterization of fluor-chlorapatites by electron probe microanalysis with a focus on time-dependent intensity variation of halogens. Am Miner 97:1103–1115

Haas JR, Shock EL, Sassani DC (1995) Rare earth elements in hydrothermal systems: estimates of standard partial molal thermodynamic properties of aqueous complexes of the rare earth elements at high pressures and temperatures. Geochim Cosmochim Acta 59:4329–4350. doi:10.1016/0016-7037(95)00314-P

Hammerli J, Kemp AIS, Spandler C (2014) Neodymium isotope equilibration during crustal metamorphism revealed by in situ microanalysis of REE-rich accessory minerals. Earth Planet Sci Lett 392:133–142. doi:10.1016/j.epsl.2014.02.018

Hand M, Sandiford M (1999) Intraplate deformation in central Australia, the link between subsidence and fault reactivation. Tectonophysics 305:121–140. doi:10.1016/S0040-1951(99)00009-8

Harlov DE, Förster H-J (2004) Fluid-induced nucleation of (Y + REE)-phosphate minerals within apatite: nature and experiment. Part II. Fluorapatite. Am Mineral 88:1209–1229

Harlov DE, Wirth R, Förster H-J (2005) An experimental study of dissolution–reprecipitation in fluorapatite: fluid infiltration and the formation of monazite. Contrib Miner Petrol 150:268–286. doi:10.1007/s00410-005-0017-8

Hellner E, Schürmann K (1966) Stability of metamorphic amphiboles: the tremolite–ferroactinolite series. J Geol 74:322–331. doi:10.2307/30062309

Hoatson DM, Jaireth S, Miezitis Y (2011) The major rare-earth-element deposits of Australia: geological setting, exploration, and resources. Geoscience Australia

Hokada T, Motoyoshi Y (2006) Electron microprobe technique for U-Th-Pb and REE chemistry of monazite, and its implications for pre-, peak- and post- metamorphic events of the Lutzow-Holm Complex and the Napier Complex, East Antarctica. Polar Geosci 19:118–151

Hussey KJ (2003) Rare earth element minerlisation in the eastern Arunta Region Northern Territory Geological Survey Record 2003–004

Hussey KJ, Tyrrell J (2012) Nolans project update. Arafura Resources Limited, Perth

Huston DL, Roland M, Hussey KJ (2011) The Nolans Bore rare earth element–phosphorous–uranium–thorium deposit: geology, age and origin. In: 11th SGA biennial meeting: let's talk ore deposits, Antofagasta, Chile, pp 127–129

Huston D, Maas R, Cross A, Hussey K, Mernagh T, Fraser G, Champion D (2015) The Nolans rare-earth element-phosphorus-uranium mineral system: geology, origin and post-depositional modifications. Miner Depos **(in review)**

Jackson SE, Pearson NJ, Griffin WL, Belousova EA (2004) The application of laser ablation-inductively coupled plasma-mass spectrometry to in situ U–Pb zircon geochronology. Chem Geol 211:47–69. doi:10.1016/j.chemgeo.2004.06.017

Košler J, Sylvester PJ (2003) Present trends and the future of zircon in geochronology: laser ablation ICPMS. Rev Miner Geochem 53:243–275

Krenn E, Harlov DE, Finger F, Wunder B (2012) LREE-redistribution among fluorapatite, monazite, and allanite at high pressures and temperatures. Am Miner 97:1881–1890

Lledo HL, Jenkins DM (2008) Experimental Investigation of the upper thermal stability of Mg-rich actinolite; implications for Kiruna-type iron deposits. J Petrol 49:225–238. doi:10.1093/petrology/egm078

Ludwig KR (2012) Isoplot/Ex Version 3.75. A geochronological toolkit for microsoft excel. Berkeley

Maas R, Huston D, Hussey K (2009) Isotopic constraints on the genesis of world-class REE-P-U-Th mineralization, Nolan Bore, Central Australia. Geochim Cosmochim Acta 73:A809

McLaren S, Sandiford M, Dunlap WJ, Scrimgeour I, Close D, Edgoose C (2009) Distribution of Palaeozoic reworking in the Western Arunta Region and northwestern Amadeus Basin from 40Ar/39Ar thermochronology: implications for the evolution of intracratonic basins. Basin Res 21:2009

Morrissey LJ, Hand M, Raimondo T, Kelsey DE (2014) Long-lived high-T, low-P granulite facies metamorphism in the Arunta Region, central Australia. J Metamorph Geol 32:25–47. doi:10.1111/jmg.12056

Orihashi Y, Si Nakai, Hirata T (2008) U–Pb age determination for seven standard zircons using inductively coupled plasma-mass spectrometry coupled with frequency quintupled Nd-YAG ($\lambda = 213$ nm) laser ablation system: comparison with LA-ICP-MS zircon analyses with a NIST glass reference material. Resour Geol 58:101–123. doi:10.1111/j.1751-3928.2008.00052.x

Pandur K, Kontak DJ, Ansdell KM (2014) Hydrothermal evolution in the Hoidas Lake vein-type REE deposit, Saskatchewan, Canada: constraints from fluid inclusion microthermometry and evaporate mound analysis. Can Mineral 52:717–744

Paquette JL, Tiepolo M (2007) High resolution (5 μm) U–Th–Pb isotope dating of monazite with excimer laser ablation (ELA)-ICPMS. Chem Geol 240:222–237. doi:10.1016/j.chemgeo.2007.02.014

Putnis A (2009) Mineral replacement reactions. Rev Miner Geochem 70:87–124

Raimondo T, Clark C, Hand M, Faure K (2011) Assessing the geochemical and tectonic impacts of fluid–rock interaction in mid-crustal shear zones: a case study from the intracontinental Alice Springs Orogen, central Australia. J Metamorph Geol 29:821–850. doi:10.1111/j.1525-1314.2011.00944.x

Read CM, Cartwright I (2000) Meteoric fluid infiltration in the middle crust during shearing: examples from the Arunta Inlier, central Australia. J Geochem Explor 69–70:333–337. doi:10.1016/S0375-6742(00)00134-5

Roberts EA, Houseman GA (2001) Geodynamics of central Australia during the intraplate Alice Springs Orogeny: thin viscous sheet models. Geol Soc Lond Special Publ 184:139–164

Rubatto D, Williams IS, Buick IS (2001) Zircon and monazite response to prograde metamorphism in the Reynolds Range, central Australia. Contrib Miner Petrol 140:458–468

Scrimgeour I (2006) The Arunta Region: links between tectonics and mineralisation. In: Annual geoscience exploration seminar, alice springs, 28–29 March 2006. Northern Territory Geological Survey

Sharp ZD (1990) A laser-based microanalytical method for the in situ determination of oxygen isotope ratios of silicates and oxides. Geochim Cosmochim Acta 54:1353–1357. doi:10.1016/0016-7037(90)90160-M

Shaw RD, Black LP (1991) The history and tectonic implications of the Redbank Thrust Zone, Central Australia, based on structural, metamorphic and Rb–Sr isotopic evidence Australian. J Earth Sci 38:307–332. doi:10.1080/08120099108727975

Shaw RD, Stewart AJ, Black LP (1984) The Arunta Inlier: a complex ensialic mobile belt in central Australia. Part 2: tectonic history Australian. J Earth Sci 31:457–484. doi:10.1080/08120098408729305

Smith MP, Henderson P, Campbell LS (2000) Fractionation of the REE during hydrothermal processes: constraints from the Bayan Obo Fe-REE-Nb deposit, Inner Mongolia, China. Geochim Cosmochim Acta 64:3141–3160

Spandler C, Pettke T, Rubatto D (2011) Internal and external fluid sources for eclogite-facies veins in the Monviso Meta-ophiolite, Western Alps: implications for fluid flow in subduction zones. J Petrol 52:1207–1236. doi:10.1093/petrology/egr025

Taylor SR, McLennan SM (1985) The continental crust: its composition and evolution. Blackwell, Oxford

Tera F, Wasserburg GJ (1972) U–Th–Pb systematics in lunar highland samples from the Luna 20 and Apollo 16 missions. Earth Planet Sci Lett 17:36–51. doi:10.1016/0012-821X(72)90257-9

Tucker RT, Roberts EM, Hu Y, Kemp AIS, Salisbury SW (2013) Detrital zircon age constraints for the Winton Formation, Queensland: contextualizing Australia's Late Cretaceous dinosaur faunas. Gondwana Res 24:767–779. doi:10.1016/j.gr.2012.12.009

Valley JW, Kitchen N, Kohn MJ, Niendorf CR, Spicuzza MJ (1995) UWG-2, a garnet standard for oxygen isotope ratios: Strategies for high precision and accuracy with laser heating. Geochim Cosmochim Acta 59:5223–5231. doi:10.1016/0016-7037(95)00386-X

Van Achterbergh E, Ryan CG, Jackson SE, Griffin WL (2001) Data reduction software for LA-ICP-MS. Paper presented at the Laser-Ablation-ICPMS in the earth sciences: principles and applications

Vry J, Compston W, Cartwright I (1996) SHRIMP II dating of zircons and monazites: reassessing the timing of high-grade metamorphism and fluid flow in the Reynolds Range, northern Arunta Block, Australia. J Metamorph Geol 14:335–350. doi:10.1111/j.1525-1314.1996.00335.x

Williams-Jones AE, Migdisov AA, Samson IM (2012) Hydrothermal mobilisation of the rare earth elements—a tale of "Ceria" and "Yttria". Elements 8:355–360. doi:10.2113/gselements.8.5.355

Wolf MB, London D (1995) Incongruent dissolution of REE-and Sr-rich apatite in peraluminous granitic liquids: differential apatite, monazite, and xenotime solubilities during anatexis. Am Mineral 80:765–775

Worden KE, Carson CJ, Close DF, Donnellan N, Scrimgeour I (2008) Summary of results. Joint NTGS-GA geochronology: Tanami Region, Arunta Region, Pine Creek Orogen and Halls Creek Orogen correlatives Northern Territory Geological Survey, Record 2008-003

Yang Y, Sun J, Xie L, Fan H, Wu F (2008) In situ Nd isotopic measurement of natural geological materials by LA-MC-ICPMS. Chin Sci Bull 53:1062–1070

Zheng Y-F (1993) Calculation of oxygen isotope fractionation in hydroxyl-bearing silicates. Earth Planet Sci Lett 120:247–263. doi:10.1016/0012-821X(93)90243-3

Zirner ALK, Marks MAW, Wenzel T, Jacob DE, Markl G (2015) Rare earth elements in apatite as a monitor of magmatic and metasomatic processes: the Ilímaussaq complex South Greenland. Lithos 228–229:12–22